Characterization of Oscillatory Lift in MFC Airfoils

Joseph R. Lang

Thesis submitted to the faculty of the Virginia Polytechnic Institute and State University in partial fulfillment of the requirements for the degree of

Master of Science
In
Mechanical Engineering

Kevin B. Kochersberger, Chair
Pablo A. Tarazaga
William J. Devenport

8/12/14
Blacksburg, Virginia

Keywords: Morphing Airfoil, Piezoelectricity, Macro-Fiber Composite, Oscillatory Lift, Smart Wing

Characterization of Oscillatory Lift in MFC Airfoils

Joseph R. Lang

ABSTRACT

The purpose of this research is to characterize the response of an airfoil with an oscillatory morphing, Macro-fiber composite (MFC) trailing edge. Correlation of the airfoil lift with the oscillatory input is presented. Modal analysis of the test airfoil and apparatus is used to determine the frequency response function. The effects of static MFC inputs on the FRF are presented and compared to the unactuated airfoil.

The transfer function is then used to determine the lift component due to cambering and extract the inertial components from oscillating airfoil. Finally, empirical wind tunnel data is modeled and used to simulate the deflection of airfoil surfaces during dynamic testing conditions. This research serves to combine modal analysis, empirical modeling, and aerodynamic testing of MFC driven, oscillating lift to formulate a model of a dynamic, loaded morphing airfoil.

Acknowledgments

The following research would not have been possible without the support of my advisors, colleagues, and family. I would first like to thank my committee chair, Dr. Kevin Kochersberger for his guidance and advice throughout my graduate work. I would not have been able to complete this research without his willingness to provide direction and his expertise in the field of morphing airfoils. Next, I would like to acknowledge my other committee members, Dr. Pablo Tarazaga and Dr. William Devenport for their commitment to my research and guidance throughout my experiments and analysis.

As a continuation of research from previous projects, I would like to thank graduate students before me who laid a foundation for me to build upon. Thanks to Dr.Onur Bilgen for building the wind tunnel that I used throughout my research and his thorough documentation of the build, calibration, and validation of his design. I would like to acknowledge both Eric Gustafson and Troy Probst for inspiring me with their research on MFC morphing airfoils.

Thank you to Bryan Joyce for his support in reassembly of the wind tunnel and assisting in the setup of some of my experiments. Next I would like to thank all of my colleagues in both the Unmanned Systems Lab and the Center for Intelligent Material Systems and Structures (CIMSS) lab. Scott Radford, Mico Woolard, Justin Stiltner, Gordon Christie, and Haseeb Chaudhry all provided some form of support throughout my research providing suggestions to enhance my experimental analysis, listening to me explain my unrelated research, and lightening the mood during numerous coffee breaks.

Finally, I would like to thank my parents, Karen and Joe Lang for their financial and emotional support throughout my undergraduate and graduate schooling. They fully backed my decision for continued education and provide invaluable advice during life's crossroads.

Contents

List of Figures

List of Tables

Chapter 1

Introduction

Recent developments in piezoelectric, smart materials show promise for morphing surface control in aerodynamic applications. The characterization of electrical/mechanical properties of smart materials lends to more accurate actuator and sensor models along with a better defined set of performance expectations. A more thorough understanding of performance characteristics will aid in specifying the advantages limitations of smart materials for specific applications.

1.1 Motivation

The motivation behind this paper is to extend on previous research and to collect experimental data on oscillatory lift in a Macro-Fiber Composite airfoil. Characterization of the frequency response properties of Macro-Fiber Composite morphing airfoils will help define performance characteristics like lag in actuator response and the applied bandwidth limitations of this technology. Although morphing airfoils are a less prevalent aeronautical control mechanism than conventional ailerons and swashplates, the potential benefits from improved aerodynamic efficiency and reduction in mechanical complexity and weight make this technology an attractive research topic.

These relatively light weight actuators are perfect candidates for use in small UAVs. Flight weight drive circuitry for MFCs has already been developed and tested on a small fixed wing UAV and been shown to have potential. Theoretical applications of morphing surfaces on rotorcraft blades helped to drive some of the testing methodology behind this research. The incorporation of sensitive laser displacement sensors into wind tunnel testing provided a gateway for modeling the oscillating camber of airfoils from collected data.

1.2 Method and Organization

This paper will begin by providing an overview of Macro-Fiber Composites and examining the actuator structure and method of inducing strain. Next, recent analysis on the

application of Macro-Fiber Composite morphing surfaces for the purpose of airfoil control will be discussed. Research on alternative oscillatory camber mechanisms for airfoil control will be presented and potential benefits and detriments to each system will be examined.

The wind tunnel test facility used to collect data will be introduced with an overview of general characteristics and specifications of the tunnel. The current equipment used to collect experimental data will be described along with calibration methods and wind tunnel corrections. Procedures for collecting wind tunnel data are then discussed with an outline of the program architecture used to collect data in each experiment. An overview of the test airfoil is described along with a brief explanation of the airfoil composition. Modal testing of the airfoil and test apparatus is presented with descriptions of resonant peaks of interest that provide answers to some of the frequency response phenomena seen during wind tunnel testing. Finally, wind tunnel test results from both static and oscillatory MFC actuation are presented and analyzed. This data is then used to create an empirical geometric model of the airfoil in Matlab to visualize the airfoil response to oscillatory inputs.

Chapter 2

Literature Review

The following sections outline pertinent research that provided both insight and direction throughout this thesis. The first section provides a background of Macro-Fiber composites (MFCs). The following section presents research on the general characterization of MFCs and the implementation of MFCs as control surfaces for a fixed wing aircraft. The final section outlines research on the application of cambering airfoils for both morphing multi-rotor control and vibration reduction.

2.1 MFC Smart Materials Overview

Macro-Fiber Composites (MFCs) are flexible, piezoelectric actuators that were developed by the NASA Langley Research Center in 1996 [1]. Macro-Fiber composite actuators are a thin patch like structure made up of rectangular piezoceramic fibers, electrodes, and polyimide film bonded together with an epoxy. Interdigitized electrodes connect the applied voltage directly to the orthogonal piezoceramic fibers. This voltage induces strain in each of the piezoceramic rods and causes the composite to actuate. A typical voltage range for an MFC is -500 to +1500V.

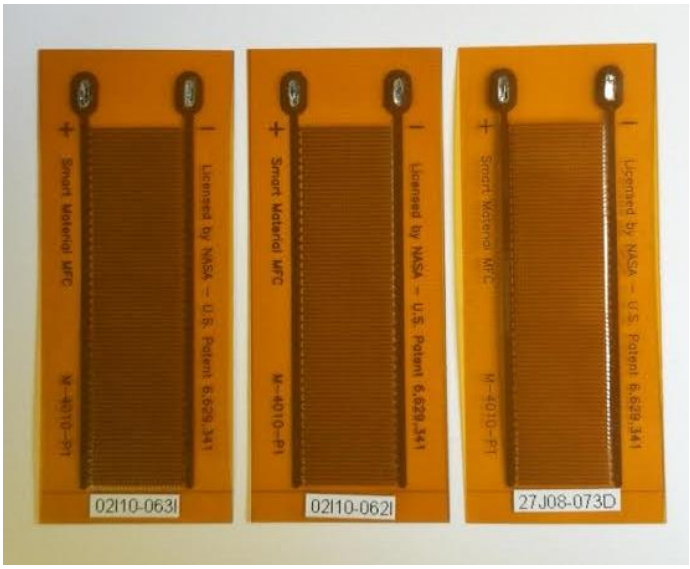

Figure 1: M4010-P1 (d33 type) Macro-Fiber Composite with zero degree fiber orientation

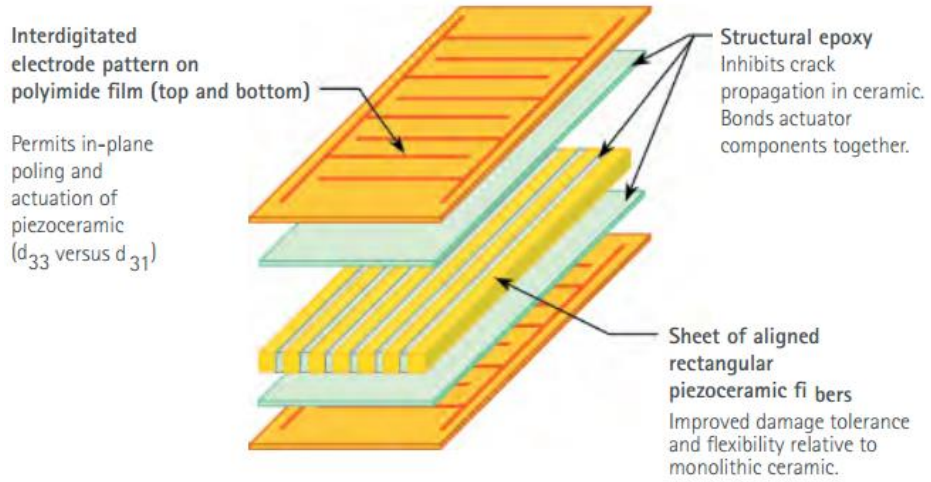

Figure 2: Structure of an MFC "smart-materials.com," Smart Material, [Online]. Available: http://www.smart-material.com/MFC-product-main.html. [Accessed 2014]. Fair Use, 2014 [1]

This relatively new piezoelectric device is an improvement on earlier piezoceramic fiber actuators due to the low cost fabrication process. The MFC piezoelectric fibers are created by machining PZT (lead zirconate titanate) wafers into fiber sheets using a computer controlled dicing saw [2]. The rectangular shape of the piezoceramic fibers was also an improvement upon the extruded cylindrical fibers of previous piezoceramic fiber composites because the flat fiber surface allowed for improved fiber to electrode contact. The robustness of this piezoelectric device allows for a relatively long actuator lifetime (typically 10^8 cycles). MFCs are currently available with either zero or forty-five degree fiber orientation.

When a voltage is applied to an MFC, it can produce in plane expansion or out of plane bending and torsion depending on how the actuator is structured. MFCs are available in d33 (elongator) and d31 (contractor) operational modes. A d33 mode MFC induces in plane strain parallel within the piezoceramic fiber while the d31 configuration induces out of plane strain normal to the MFC plane within the piezoceramic [1]. The d33 mode aligns the electric field with the direction of strain taking advantage electromechanical coupling. This coupling provides for a steeper strain/energy curve than that of the d31 mode MFC [3]. For this reason, d33 mode MFCs are typically used due to the high electromechanical efficiency associated with that configuration.

MFCs have several desirable characteristics for implementation in control surfaces including high strain energy density, directional actuation, conformability, high bandwidth, ability to bond to non-planar geometries, and durability [2]. The inherent flexibility of an MFC

allows it to be bonded to curved surfaces unlike many monolithic piezoceramic materials. This conforming property makes MFCs an excellent candidate as an actuator for a variety of applications like vibration suppression, morphing surfaces, and flow control. In addition to being extremely flexible, MFCs have a relatively high unloaded bandwidth in comparison to conventional servos allowing for fast response time when used in control applications. MFCs can also be used in converse for applications like an energy harvesting device, or an extremely sensitive strain gauge due to their ability to produce higher voltages.

When MFCs are used as an actuator they are typically used in either a unimorph or bimorph configuration. The unimorph configuration uses a single MFC bonded to a substrate to provide voltage induced strain. This simplistic implementation of an MFC benefits from minimal weight and driver circuit complexity. A bimorph configuration uses two MFCs bonded to a substrate, providing a larger strain input than a unimorph configuration. Bimorph configurations are driven by producing a positive strain in the piezoceramic fibers of one MFC while simultaneously producing a negative strain in the piezoceramic component in the second MFC.

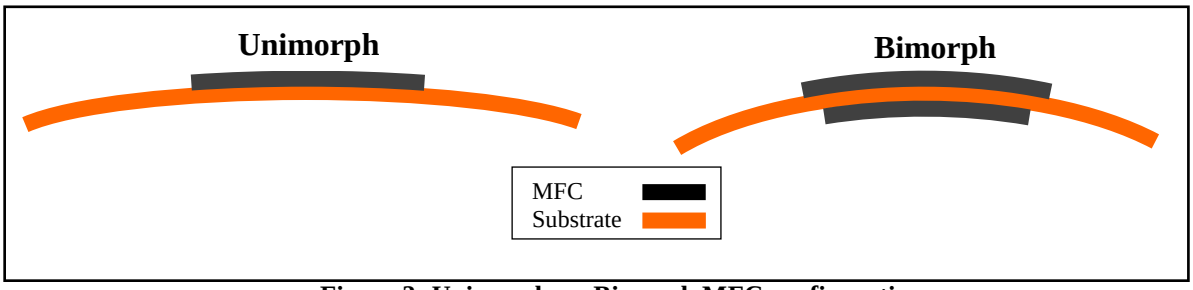

Figure 3: Unimorph vs. Bimorph MFC configuration

The addition of a second MFC introduces both weight and driver circuit complexity due to the asymmetric voltage necessary to drive this configuration. In order to provide +100% actuation, the supply voltage required to the upper and lower MFC is +1500V and -500V respectively. Methods of segmenting high voltages to drive a bimorph configuration will be described in section 5. Figure 4 shown below represents voltage requirements in order to fully actuate a bimorph.

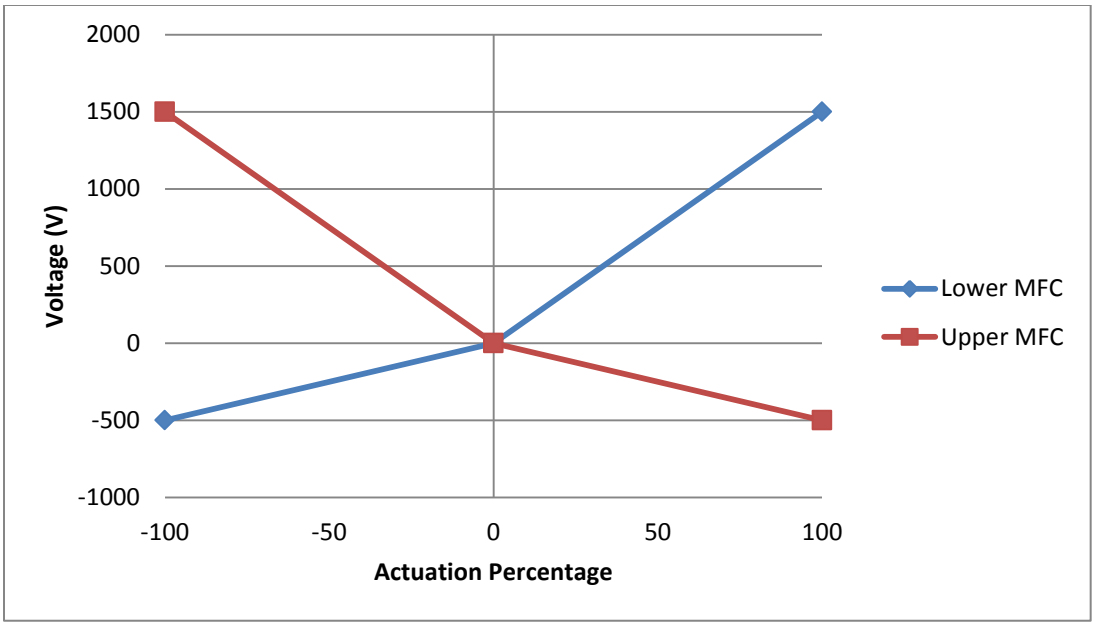

Figure 4: MFC Voltage vs Actuation percentage for a typical d33 mode bimorph configuration

2.2 MFC Morphing Control Surfaces

Research on the characterization, design, and implementation of MFCs in embedded airfoils is relatively new because MFCs were developed in 1996. The low cost of production, high bandwidth, and high strain energy density properties of MFCs contribute to making them candidates for morphing control surfaces.

Bilgen [3] began his research characterizing smart materials for morphing control applications and cited benefits to using MFCs over other piezoceramic materials, specifically in a d33 mode. He experimented with MFCs in unimorph and bimorph configurations for morphing airfoil camber and flow control. During these experiments he developed a novel circuit capable of driving two MFCs in a bipolar/bimorph configuration. This circuit allowed a bimorph configuration of MFCs to be actuated throughout their full actuation range. A comparison of actuation configuration options is outlined in detail in Bilgen's thesis and his circuit is used to drive experimental airfoils throughout this paper.

Bilgen extended his research experimenting with active flow control through mean camber line oscillations. He constructed a variable camber NACA0010 airfoil with nine unimorph MFCs on the leading edge to control the camber line. Bilgen tested the aerodynamic response by oscillating the airfoil symmetrically with all nine MFCs and asymmetrically with only some of

the actuators. By oscillating the leading edge of this test airfoil, Bilgen was able to increase the lift coefficient in the post stall region by 27.5% while actuating the leading edge at 125 Hz with a flow rate of 5 m/s.

Gustafson [4] studied the structural properties of laminate composites for thin profile MAV morphing wing design. He developed an FEA model of MFCs using a thermal analogy for piezoelectric strain. Using this model he simulated the deformation, lift, and drag characteristics of a novel thin GenMAV airfoil with MFC morphing camber. Gustafson later constructed this airfoil for wind tunnel testing to compare with his model. Through 2D wind tunnel testing, he measured aerodynamic loading under static deflections along with lift and drag. As a further proof of concept that MFC bimorph implementation in a MAV was feasible, Gustafson developed a flight weight circuit capable of driving MFC bimorphs that only weighed 23 grams.

Probst [5] expanded on Gustafson's research and compared an airfoil with trailing edge MFC camber control to conventional servomechanism ailerons used on UAVs. Theoretically, the MFC camber controlled airfoil should have been more efficient than the servomechanism due to the continuous surface contour. Probst's experiments showed the servomechanism achieved a higher L/D efficiency but noted that the MFC was not actuating at the same camber percentage as the servomechanism. He noted that the aeroelastic deflection of the loaded MFC airfoil changed the overall camber to be less than that of the servomechanism.

Probst rapid prototyped a continuously cambered airfoil (resembling the MFC airfoil) and a conventional actuated aileron shape airfoil. The rapid prototyped airfoils were sufficiently stiff enough that aerodynamic loading did not alter the contour of either airfoil. After rerunning his experiment, Probst found that the continuous airfoil was more efficient. Probst mentioned a need to take aeroelastic effects into account during the design of MFC control surfaces to correct for changes in camber due to aerodynamic loading. After wind tunnel tests, Probst simulated a thin wing with MFC's in different configurations. He used a FEA to determine the optimal location and configuration MFCs control surfaces for roll authority. Probst, along with researchers from AVID LLC constructed and tested this thin winged design and compared it to the simulated results.

Kim and Han [6] developed a flight mechanism with MFCs morphing control surfaces in an ornithopter configuration to mimic the flight mechanisms of birds and insects. The MFCs

provide a camber control input into the flapping wing design while an electric motor creates the flapping motion. Kim and Han experiment with various flapping frequencies and air speeds. They show that the lift generated by the flapping wing can be increased by 20% when the MFCs camber control is included in the flapping wing vehicle.

2.3 Alternative Oscillatory Camber Mechanisms

Research to use oscillatory surfaces on helicopter rotors for the purpose of harmonic control is not new. Duffy, Nickerson, and Colasante [7] experimented with a 12 percent thick modified VR-7 airfoil from a four foot section of the Boeing CH-47 Chinook helicopter blade to evaluate the feasibility of a higher harmonic control surface embedded in a rotor. The snap through airfoil design had a pneumatic actuator and two bar linkage on the interior that altered the lower airfoil surface aft of the D box by snapping the lower surface in toward the centerline of the airfoil. A preliminary second order vortex panel analysis of the airfoil showed the snap through mechanism was capable of increasing the coefficient of pressure across the airfoil and subsequently the lift and nose-down pitching moment.

After integrating the pressure coefficient over the airfoil surface at various angles of attack, Duffy determined that direct cyclic pitch control via the snap through mechanism and a rigid rotor blade was not possible because the coefficient of lift only increased by 0.06 when the mechanism was fully actuated compared to the unactuated airfoil. After integrating the load distributions along the rotor blade, Duffy found that the reduction in lift due to the twist induced in the rotor blade from the nose down pitching moment dominated the slight increase in lift due to the camber change in the snap through airfoil. Although the snap through panel mechanism could not be used to control the rotor directly, it was found that the elastic twist induced in the rotor from the nose-down pitching moment effectively reduced the overall blade lift, and this reduction in overall blade lift could potentially be used for cyclic control.

Oscillatory morphing of the airfoil camber line has also been used for wake vortex mitigation and active control of airfoil flow separation. Pern and Jacob [8] utilized a modified NACA 4415 airfoil with a THUNDER piezo-ceramic actuator mounted beneath the surface of the airfoil to modify the curvature of the upper surface $\pm 0.2mm$. Pern conducted preliminary

experiments on this airfoil, measuring the velocity deficit and vorticity fields in an initial study of the airfoil's potential for wake vortex mitigation.

Munday and Jacob [9] expanded on this work measuring force and particle image velocimetry of the airfoil in static conditions with intermediate and maximum upper surface displacements which resulted in a L/D decrease of 6% and increase in 2% respectively. After preliminary testing, they oscillated the upper surface at frequencies between 0 and 11 Hz in low Reynolds number conditions at various angles of attack. Through smoke wire flow visualization they were able to show that oscillating the curvature of the upper surface effectively reduced flow separation by as much as 30-60% at angles of attack up to 9 degrees. He notes that the point of flow separation is comparatively the same between both the actuated and unactuated cases and that since the region of camber oscillation is downstream of the separation point, the actuation in not affecting the upstream flow directly. They theorized that the surface oscillations are aiding the flow in navigating the adverse pressure gradient in the separation region by energizing the boundary layer.

Clement [10] conducted a bench top and preliminary wind tunnel analysis of an active rotor blade flap. He constructed a modified twelve inch NACA 0012 airfoil with a trailing edge flap as the platform for his experiments. Actuation of the rotor flap was conducted using a novel structure of C-Block piezoelectric actuators stacked horizontally within the rotor body. These actuators provide deflection of the trailing edge flap that is 10% of the chord through a series of brass shims. The C-Block actuators provided small trailing edge flap deflections with a maximum deflection of approximately 100 μm recorded corresponding to 6 degrees of angular deflection. Maximum blocking forces of approximately 10 N were recorded for the trailing edge while actuating the trailing edge and simultaneously forcing the trailing edge to return to zero deflection. Clement mentions the need for precise location of the center of pressure on the spar axis to reduce an induced moment in the airfoil.

Garcia [11] created a state space model for a helicopter rotor with blade mounted actuators and evaluated the use of servo flaps for higher harmonic control in helicopter blades. Garcia's state space model is based on the use of Multi-Blade Coordinates (MBCs) and a lumped torsional approximation of each rotor blade. He validated this state space model using Boeing's C60 aeroelastic rotor analysis program. Garcia characterized requirements for a HHC system by determining the servo-flap loading and deflection for 0.25g of HHC authority. He compares this

actuation scheme to the HHC loading and deflection of a conventional root pitch control mechanism. Garcia goes on to explain the extreme benefit of using servo-flaps for HHC rather than root pitch actuation is the reduction of control loads necessary for vibration suppression. Finally, he presents a multivariable linear quadratic regulator in conjunction with his rotor model that could be used for HHC.

Straub and Merkley [12] developed plans and actuator requirements for a servo flap mechanism to camber rotor mounted servo flaps. Using typical flight conditions for an AH-64 helicopter, they developed a set of physical target requirements for linear and torsional loading factors, cyclical actuation rate, thermal environmental conditions, ruggedness, power requirements, weight, and size. In addition to creating a list of physical target specifications, qualitative design constraints like ease of maintainability are considered. The proposed design for the servo flap mechanism consists of a linear actuator mounted in the plane of the blade spar combined with a hydraulic piston to actuate the blade mounted flap. Smart materials considered for the linear actuator include piezoelectric stack actuators, magnetostrictive, and shape memory alloys (SMAs).

Chapter 3

Wind Tunnel Facility

The following section describes the wind tunnel test facility used to collect data for all aerodynamic experiments. A summary of test equipment, calibration methods, data acquisition, and test procedure is provided. The test airfoil is described and a summary of the construction process is provided. Correlation of the airfoil lift with the oscillatory input is presented and discussed. The method of determining the lift component due to cambering is explained.

3.1 Wind Tunnel Overview

The wind tunnel used for all aerodynamic experiments presented in this research is an open circuit, low air speed, apparatus tunnel built by Bilgen specifically for testing of piezoelectric morphing airfoils and piezoelectric induced flow control as part of his PhD dissertation. This apparatus is located in the CIMSS lab of Durham Hall at Virginia Polytechnic Institute and State University and has also been used in experiments by both Gustafson and Probst to collect experimental data for Macro-Fiber Composite embedded airfoils. The tunnel body spans 4.1m in length and is constructed primarily of HVAC ducting and acrylic material.

Wind speeds from 2 m/s to 22 m/s are attainable with two cascaded AC fans that pull air through a honeycomb flow straightener at the converging inlet of the wind tunnel. Air speed is adjusted with a variable transformer to the desired speed at the beginning of each experiment. Stability of the flow speed is dependent on the magnitude of the flow speed. This is described in more detail in section A3 of the appendix. An acrylic test section that measures 136 mm tall by 365 mm wide allows for laser displacement measurements of the airfoil at multiple points on the chord span and photography during MFC actuation. The acrylic also provides a smooth inner surface to further mitigate undesirable turbulence at this critical section of the wind tunnel. A seven inch diameter portal on both the ceiling and floor of the test section allow access into the test section to install test samples.

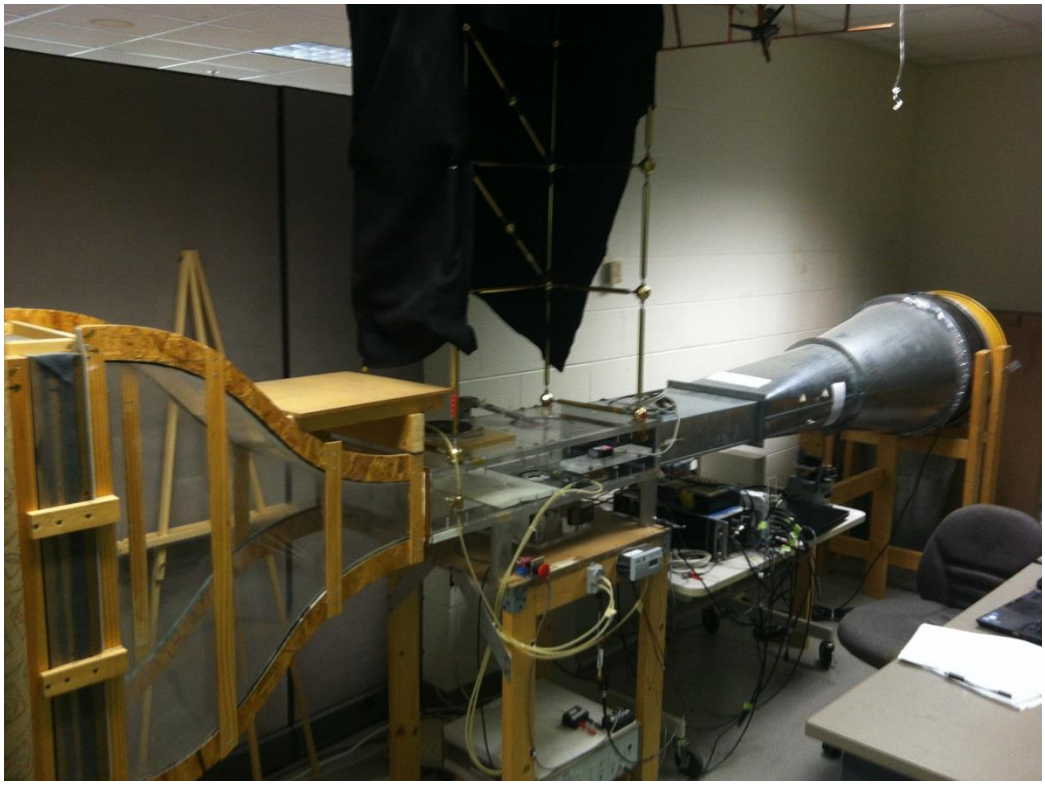

Figure 5: CIMSS Lab open circuit, subsonic wind tunnel

Static and dynamic pressure is measured using Sentra and Dwyer pressure transducers respectively. These transducers come calibrated from the factory and were verified by Gustafson using a Dwyer inclined differential manometer with +/- 0.1" water column accuracy. The Setra pressure transducer has a water-column range of 0-2.5 inches with $\pm 0.25\%$ full scale accuracy and the Dwyer transducer has a 0-5 inch water-column range with $\pm 1\%$ full scale accuracy. A J-type omega thermocouple and CCT-22 thermocouple signal conditioner are used to account for temperature variation and provide a more accurate estimate of air density during each experiment. Pitot tube static pressure at the quarter chord location is calibrated using a ratio of the pitot tube static pressure to the Setra static port pressure [3]. This static pressure ratio was used to scale the pitot static pressure and correctly account for the pressure drop at the quarter chord location.

The airflow turbulence intensity of the current wind tunnel setup with an empty test section was measured by Bilgen [3] using a standard constant temperature anemometry (hot wire anemometry) technique. Turbulence intensity is a function of the airspeed but does not exceed 0.4% for the airspeeds used throughout this research. Bilgen also measured the flow velocity

variation and found the velocity varied 4.5% horizontally and 1.5% vertically [4]. More information can be found on the measurements that Bilgen [3] made and modifications that were made to the wind tunnel in order to further mitigate turbulence in his PhD thesis paper.

Airfoil lift is measured using a Transducer Techniques MLP-10 load cell with a 10 lb measurement range and a TMO-2 signal conditioner with a combined bandwidth of 160 Hz. One side of the load cell is attached to an acrylic base and the other side is attached to an aluminum mounting bracket oriented 90 degrees from the air flow direction. This bracket is secured to a universal joint with an aluminum standoff that protrudes up into the test section to hold the airfoil. The load cell is calibrated with precision masses and a low friction pulley system attached to the side of wind tunnel. A calibration curve for the lift load cell can be seen in section A2 of the appendix. The dynamic response of the load cell measurement support system is characterized by modal testing of the airfoil and test apparatus. FRF functions for trailing edge displacement and lift force are recorded and discussed in detail in chapter 5.

Mueller and Burns [13] show that a gap between the wall and airfoil less than 0.5% of the span is usually acceptable and has a minimal effect on wind tunnel results. The gap between the airfoil and CIMSS wind tunnel wall is approximately 1.13% of the span. Bilgen describes the effects of this small yet larger than recommended gap size in his dissertation. Bilgen [3] determined tunnel wall and buoyancy corrections necessary to obtain the correct coefficient of lift and coefficient of drag from the load cell measurements. The method used to determine the corrected lift and drag coefficient is described more thoroughly towards the end of this section. Experiment control and data collection are handled using a National Instruments 6062E DAQ card. This data acquisition device is controlled by a laptop running National Instruments Labview 2009 and Windows XP. All analog input and output pins are connected to the 6062E DAQ card via a National Instruments SCC68 breakout box that provides ease of accessibility to the dense pinout on the National Instruments cable connected to the DAQ card. A connection summary of the SCC68 breakout box is provided in Table 1. The 6062E has a 12 bit ADC and 8 differential or 16 single ended analog inputs capable of 500 KS/s.

MFCs are driven using a Trek 623B high voltage bipolar amplifier capable of ±2kV with a slew rate of 300V/μs. The Trek high voltage amplifier is segmented into +1500V and -500V by a novel solid-state, asymmetric voltage divider designed and constructed by Bilgen during his research and described in detail in his PhD dissertation. This circuit allows a bimorph

configuration of MFCs to be driven from a single amplifier. A signal voltage from Labview is used to scale the amplifier output voltage to provide variations in output amplitude.
In order to collect wind tunnel data while also actuating the airfoil MFCs, the Labview VI architecture necessary to run the wind tunnel was reconfigured on a new laptop and modified to send an actuation signal while simultaneously collecting data from all of the sensors used in the experiment. Camber oscillations are produced by implementing the amplifier control signal as a sine wave with a user specified amplitude and frequency.

Table 1: SCC68 (DAQ 6062E) Connection Summary

Channel	Device	Description/Purpose
AI/0	Sentra 267 Pressure Transducer	Static port pressure
AI/1	Omega CCT-22 Thermocouple Signal Conditioner	J-type thermocouple, air temperature for density estimation
AI/2	Trek 623B High Voltage Amplifier	MFC input actuation voltage measurement
AI/3	OptoNCDT ILD 1800-200	Laser displacement measurement of airfoil surface
AI/4	Dwyer 668-5	Pitot-Static tube pressure transducer
AI/5	Transducer Techniques MLP-10, TMO-2	Lift force load cell signal conditioner
AI/6	NA	NA
AI/7	Trek 623B High Voltage Amplifier	MFC actuation current measurement
AO/0	Trek 623B High Voltage Amplifier	High voltage output for driving MFCs
D/3	Canon S5IS Camera	Test section photos

3.2 Wind Tunnel Experiment Procedure

Prior to each experiment, the airfoil angle of attack was verified using an angular reference diagram fixed below the airfoil. The alignment of the load cell balance apparatus holding the airfoil is checked to ensure the lift load cell is perpendicular to the direction of flow. Image capturing of the airfoil is setup for experiments when this feature is desired.
The Labview VI used for dynamic testing begins by initializing all input and output pins. Limits are set on critical signals like the signal to the MFC amplifier to ensure no damage can be done to the test airfoil by overvoltage. Next, the VI verifies that the fan and MFC amplifier are completely off and collects a set of data to tare all sensors prior to the experiment. The VI then

asks for the user to input a voltage amplitude and actuation frequency for the MFCs as well as the desired airspeed.

After setting up the experiment conditions the user manually sets the airspeed to the desired value using a variable transformer and starts the experiment. Data is collected and saved to a folder based on the time and date of the experiment and then subdivided into folders based on air speed, MFC actuation frequency, and amplitude. Finally, a post experiment set of data is collected to verification all sensors did not deviate significantly from the initial tare. Additional settings to automatically take photographs at various points during the experiment and to collect hysteresis data after the experiment is complete are also included for convenience.

Limitations on the test section dimensions create boundary conditions that do not accurately represent free stream conditions. Since airflow around the airfoil does not perfectly represent free stream conditions, a correction factor (k_{CL}) is included when calculating the coefficient of lift. The corrected lift coefficient when this factor is included is defined as follows:

$$C_l = k_{Cl} C_{lu} \tag{E3.1}$$

Where: C_l: Coefficient of Lift

C_{lu}: Uncorrected Coefficient of Lift

k_{Cl}: Correction factor

The lift coefficient correction factor described by Barlow [14] is similar to the method of images, where singularities are arranged to simulate real wall boundaries in a flow field. The described correction method is documented and has been used by both Bilgen [3] and Gustafson [4] in their research. The uncorrected lift coefficient is calculated using the standard lift equation shown below.

$$C_{lu} = \frac{2L}{\rho v^2 S} \quad \text{(E3.2)}$$

Where: C_{lu}: Uncorrected Coefficient of Lift

L: Lift Force

ρ: Air Density

S: Airfoil Planform Area

v: Airspeed

The correction factor is calculated via solid ϵ_{sb} and wake blockage $\epsilon_{\omega b}$ terms that account for a variation in free stream airspeed due to the volume of the airfoil and the downstream wake respectively [15]. The solid and wake blockage terms were measured by Probst [5] using the same wind tunnel and airfoil.

$$k_{Cl} = 1 - \sigma - 2\epsilon_{sb} - 2\epsilon_{\omega b} \quad \text{(E3.3)}$$

Where:

k_{Cl}: Coefficient of lift correction factor

σ: Wind tunnel correction parameter

ϵ_{sb}: Solid Blockage term

$\epsilon_{\omega b}$: Wake blockage term

A streamline curvature correction for the angle of attack is included to account for variation in the incidence angle of freestream flow do to the presence of the airfoil within the wind tunnel [15]. This correction is implemented using XFOIL data obtained for the moment coefficient. The following equation outlines the streamline curvature correction where α_{sc} is the streamline curvature correction and C_m is the moment coefficient at the quarter chord for each static actuation test of the airfoil. This correction factor is added to the angle of attack in the results found in section 6 to better represent wind tunnel test conditions.

$$\alpha_{sc} = \frac{\sigma}{2\pi}(C_{lu} - 4C_m) \quad \text{(E3.4)}$$

Where:

C_{lu}: Uncorrected Coefficient of Lift

C_m: Moment coefficient at quarter chord

σ: Wind tunnel correction parameter

α_{sc}: Streamline Curvature Correction

The streamline curvature correction and the corrected coefficient of lift are both partially made up of a wind tunnel correction parameter that relates the ratio of the chord to the wind tunnel height. This correction parameter is listed in the equation below.

$$\sigma = \frac{\pi^2 c^2}{48h^2} \quad \text{(E3.5)}$$

Where:

σ: Wind tunnel correction parameter

h: Test section height

c: Chord length

Three dimensional flow corrections for the finite width of the airfoil's vertical span were not incorporated in the following analysis. As a result, at higher coefficient of lift configurations there is more error associated with the measured coefficient of lift. This is due to a steeper gradient in the elliptical lift distribution of a finite airfoil that results from a high coefficient of lift configuration [16].

Chapter 4

Test Airfoil

4.1 Test Airfoil Description

The airfoil used for testing is a Selig S1210 high lift, low Reynolds number asymmetric airfoil. The upper surface of the trailing edge is made up of two 8541 MFCs bonded to 1 ply of 3 oz./yd^2 fiberglass oriented $\pm$45 degrees, with a 0.5 inch wide 10 oz./yd^2 carbon fiber trailing edge stiffener. The lower skin is composed of 1 ply of 3 oz. fiberglass oriented $\pm$45 degrees, with an inner ply of isotropic carbon veil. This semi flexible lower surface serves as a wiper to preserve the airfoil profile during actuation.

General dimensions of the airfoil construction can be seen below in Figure 6. A stud protrudes from the airfoil quarter chord for convenient attachment to load cell apparatuses in wind tunnel testing. This airfoil was constructed by AVID LLC [17] and used in Probst's research [5] comparing conventional servo actuated control surfaces with piezoelectric control surfaces on unmanned aerial vehicles.

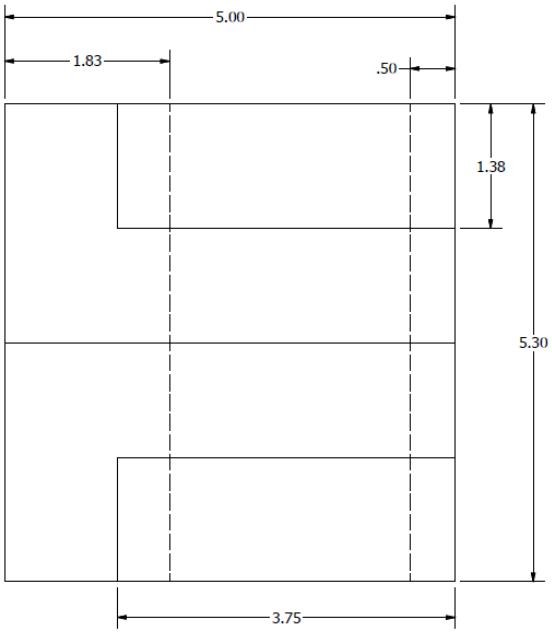

Figure 6: General Airfoil and MFC dimensions

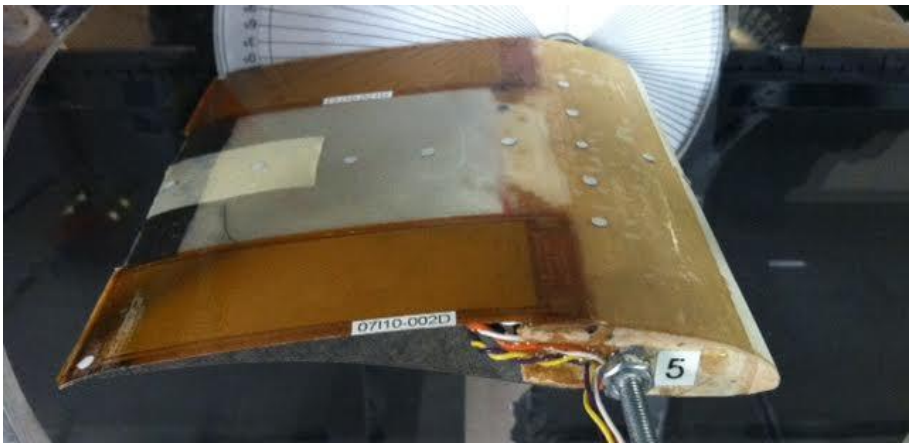

Figure 7: Selig S1210 high lift, low Reynolds number with 8541 MFC bimorph trailing edge

This bimorph MFC upper surface is capable of producing an additional positive and negative six degrees of camber into the airfoil profile. Figure 8 shown below demonstrates -100% actuation on the left and +100% actuation on the right. Positive actuation corresponds to a higher C_L profile whereas negative actuation results in a more streamlined profile.

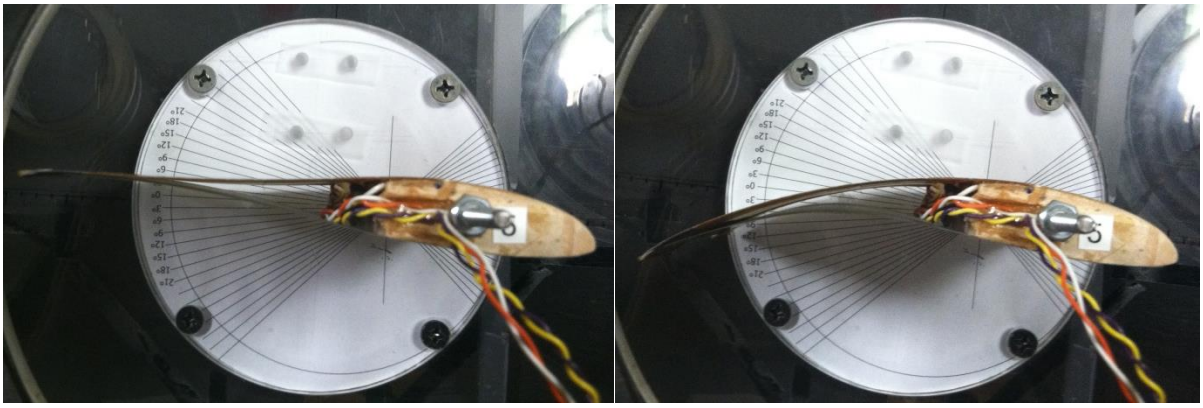

Figure 8: -100% actuation (lower left), +100% actuation (lower right)

4.2 Hysteresis Characteristics

One characteristic of piezoelectric actuators that creates complications for implementing them in control surface and sensing applications is the presence of nonlinear hysteresis. The output of a device with hysteresis depends on both the history of the previous input and the current input. Hysteresis is a rate-independent nonlinearity caused by variations in the path that voltage induced mechanical strain takes upon charging and discharging [18], [19]. In order to

prevent actuation errors, control systems must include a compensator to account for hysteresis in the control systems architecture. The use of hysteresis operators like Preisach and Prandtl-Ishilinskii for real time hysteresis compensation in control systems is a prevalent research topic [20], [21]. Compensation algorithms implemented in series with piezoelectric actuator models can produce relatively accurate linear models that are sufficient for many applications [22]. Figure 9 shown below is hysteresis of the test airfoil's trailing edge measured across a voltage loop. Note the relative precision at $\pm 100\%$ actuation and the potential for error at lower actuation percentages. Lower actuation percentages show a lack of repeatability for a given input and can yield different outputs depending on the previous history of inputs to the airfoil.

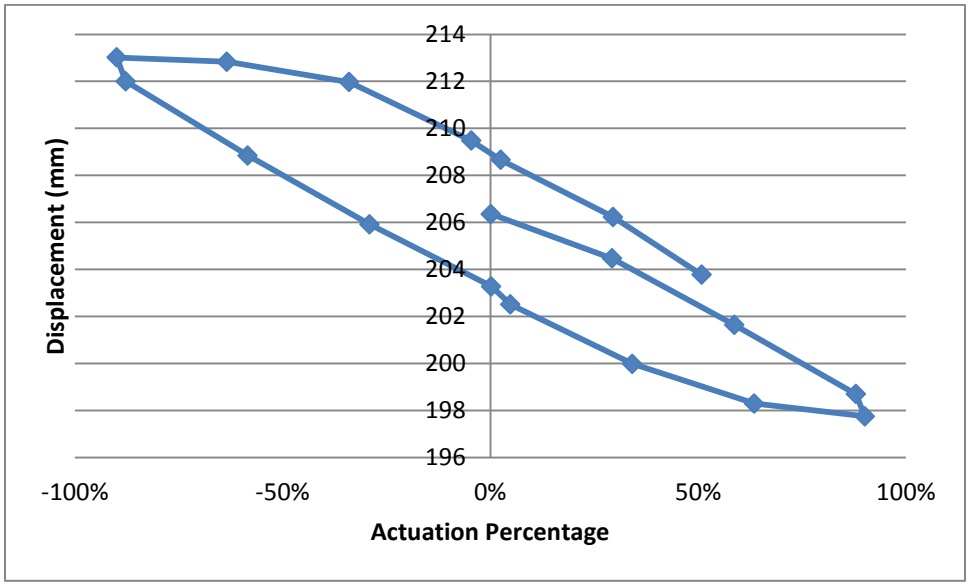

Figure 9: Trailing edge displacement hysteresis from Selig S1210 high lift MFC airfoil

Actuation cycles from one extreme to the other are relatively well known but the direction i.e. from +100% to -100% or from -100% to +100% varies the intermediate actuation characteristics of the airfoil. This directional method using one extreme percentage as an initial starting point to preload the strain in the airfoil MFCs is used when conducting experiments on the aerodynamic loading of the trailing edge to provide for a steeper actuation/displacement curve and help idealize the desired results.

4.3 Definition of Support Angle

Actuation inputs to the MFC trailing edge of the airfoil change the airfoil camber line which also changes the angle of attack. This complication makes it difficult to use the angle of attack as a parameter when analyzing data from a dynamic, oscillatory airfoil.

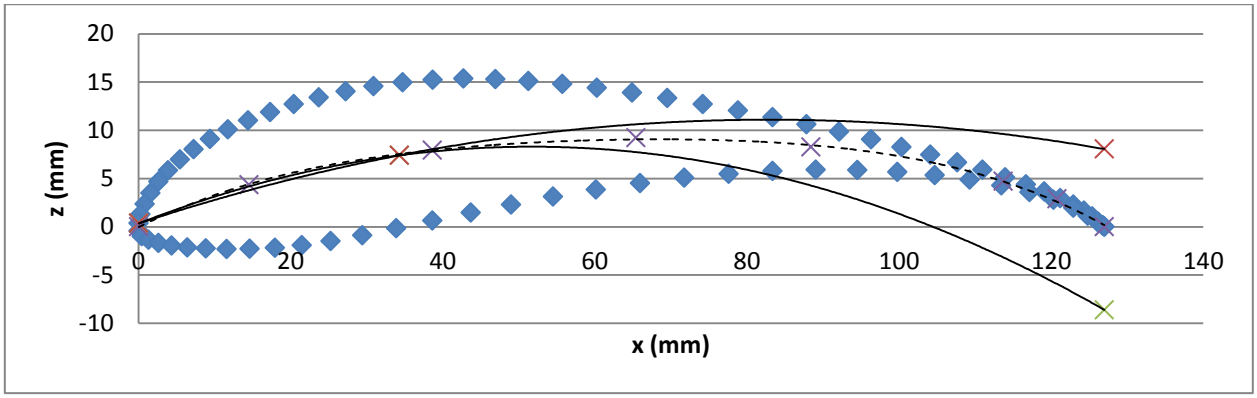

Figure 10: Variation of Airfoil Camber with MFC Actuation

For this reason, it is necessary to define a parameter that describes the initial, unactuated orientation of the airfoil with respect to the direction of free stream air flow. This initial orientation will be defined throughout this paper as the support angle (β). This angle is equivalent to the angle of attack when the MFCs are not actuated. During positive actuation the angle of attack is greater than the support angle and during negative actuation the angle of attack is less than the support angle. The support angle will allow for a better understanding of test results in the following sections and provide a metric for comparison between different initial airfoil orientations. Additional camber is determined from the airfoil trailing edge deflection using the following equations where θ_C is additional camber from the MFC deflection.

$$\theta_C = tan^{-1}\left(\frac{z_{te}}{C}\right) \qquad \text{(E3.6)}$$

$$\alpha = \beta + \theta_C \qquad \text{(E3.7)}$$

Figure 11 below shows the relationship between the angle of attack α and the support angle β for an unactuated airfoil (left) and a positively actuated airfoil (right).

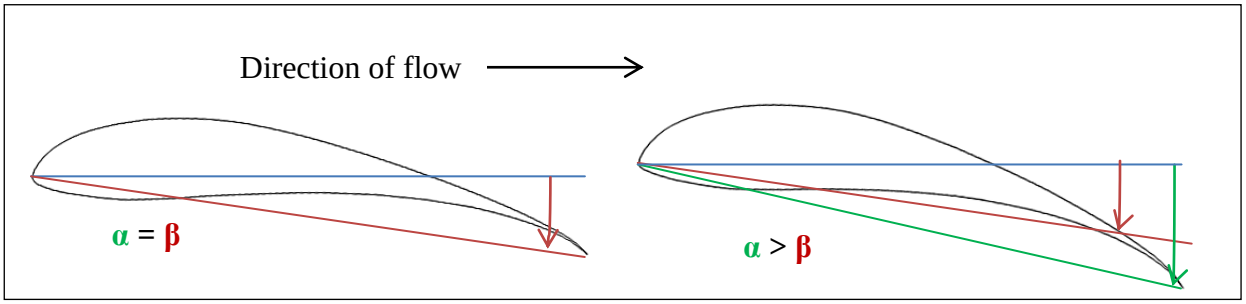

Figure 11: Relation between Angle of Attack and Support Angle for an airfoil with no actuation and an airfoil with a positive actuation percentage

Chapter 5

Modal Testing

This section describes the experimental procedure for modal testing of the airfoil and the wind tunnel measurement apparatus used to collect lift data. Modal testing of the airfoil was conducted prior to testing the airfoil in the wind tunnel. The goals of modal testing were both preventative and exploratory. One objective of the modal analysis was to highlight resonant frequencies to prevent coupling of the MFC actuators with the airfoil dynamics which could lead to destructive behavior of the test airfoil. Another goal was to explore mode shapes of the test airfoil and load cell apparatus to better understand the frequency response results from wind tunnel testing. Finally, the effect of static MFC actuation on the shape of the frequency response function is presented.

5.1 Modal Testing Description

The frequency response function of the combined airfoil and test apparatus was measured by applying an impulse to the airfoil with a modal hammer and measuring the velocity of the airfoil with a laser doppler vibrometer. Impulses were provided by a Dytran model 5800SL, Ultra Miniature Impulse Hammer at the quarter chord and 50% vertical intersection. This location is on the basswood of the airfoil and provides a better surface to excite modes of the airfoil than the composite trailing edge. Velocity was captured using a Polytech PDV 100 set at 500 mm/s/V and recorded using SigLab, a data acquisition unit designed to interface seamlessly with Matlab.

Figure 12: Polytec Portable Doppler Vibrometer (PDV) 100

Each hammer hit was verified to have a clean single impulse prior to averaging and removed if signs of multiple hits were detected. The impact placement of the hammer was moved to various locations and found to have little effect on the shape and resonant frequencies of the resulting FRF. In order to minimize the frequency attenuating effects of a massive load cell balance, the turntable and C-arm used in previous research to automate the airfoil angle of attack was removed and a new bracket to connect the lift load cell was fabricated.

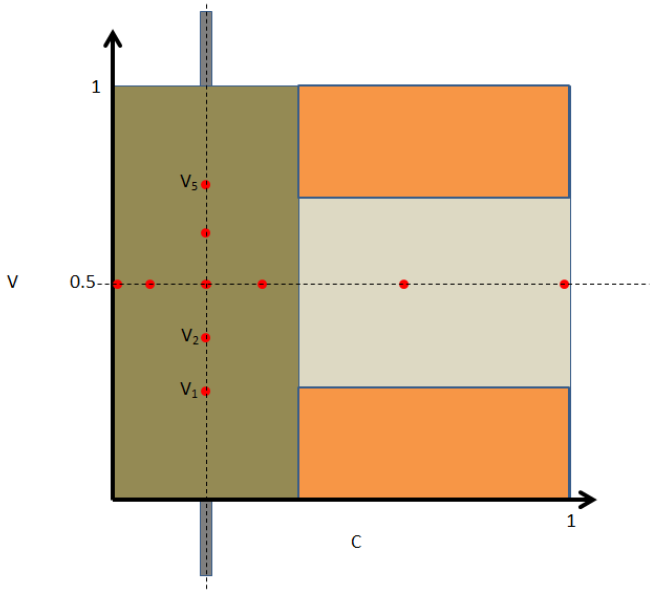

Figure 13: Modal test airfoil measurement points

5.2 Modal Test Results

Modal testing of the composite airfoil resulted in three distinct peaks. The following figures show laser measurements at various locations, spanning both the chord and the width of the airfoil. Figure 14 shows the velocity magnitudes increase with a higher percentage of vertical laser positioning. This is to be expected because the airfoil is fixed in the measurement apparatus closer to zero percent. Apart from the magnitude difference, the resulting FRFs have the same general shape. All of these measurement points were taken at the quarter chord location on the basswood leading edge of the airfoil.

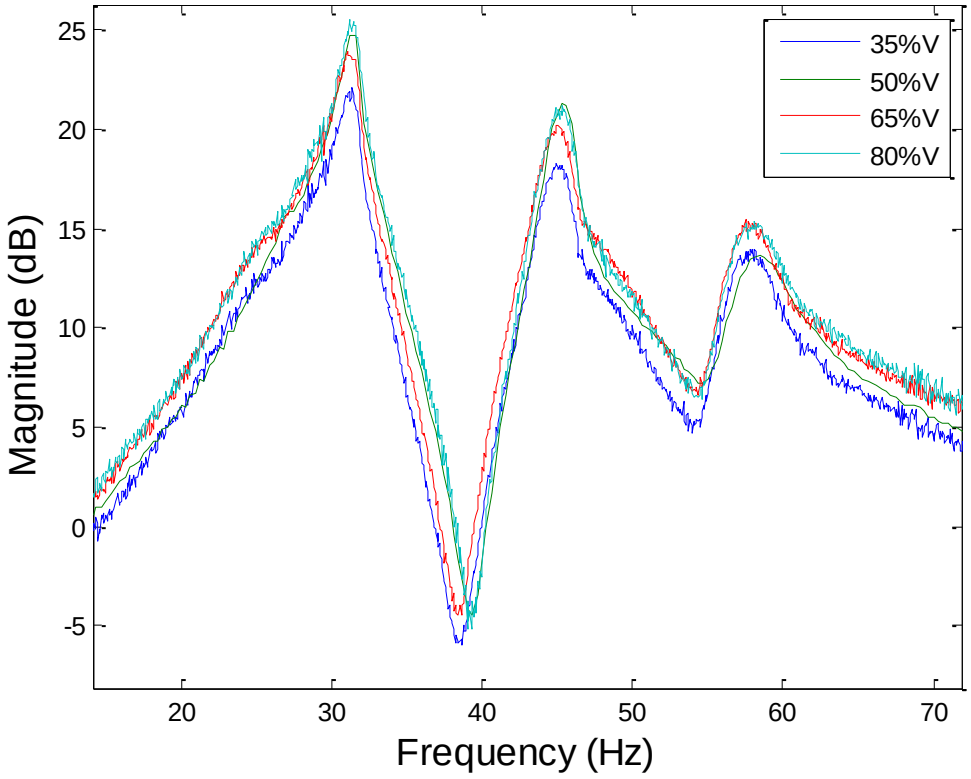

Figure 14: Frequency response function vertical comparison

Magnitude plots of modal testing across the chord of the airfoil produced a general shape that is similar to the vertically spanning measurements above. The frequency response of the trailing edge is significantly different from the other points measured on the airfoil. Absence of the antiresonance that shows up at the other measurement points is due to the large amount of

mechanical damping associated with the flexible composite trailing edge. The antiresonance location also changes slightly with variations in the chordwise measurement location. Peak locations do not change significantly when the measurement location on the chord changes.

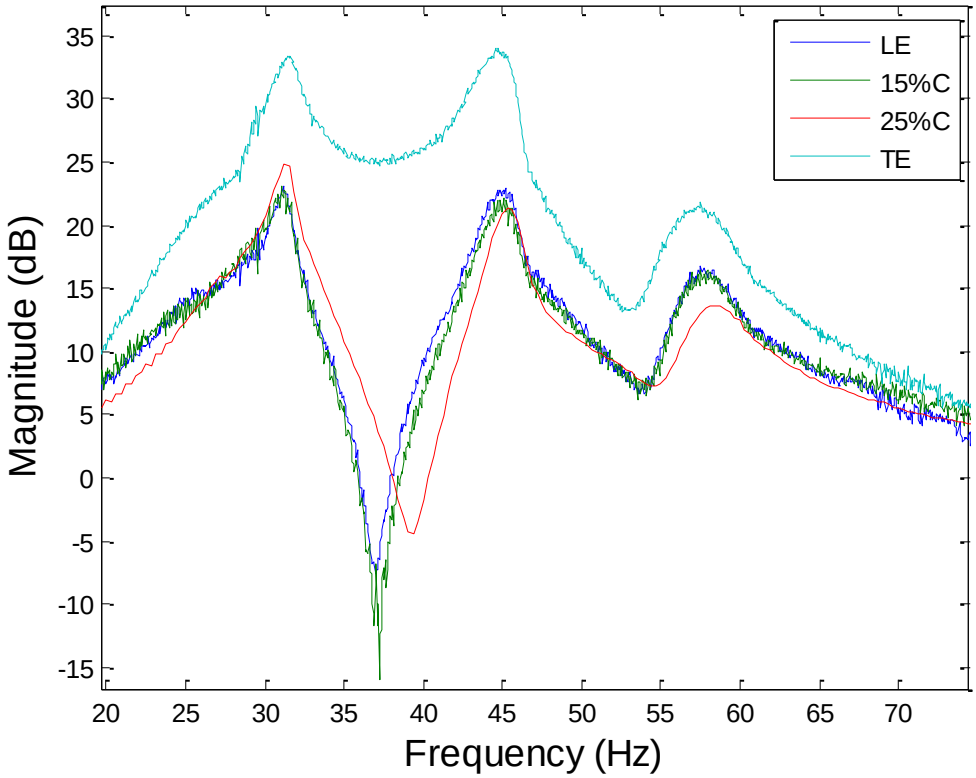

Figure 15: Frequency response function chordwise comparison

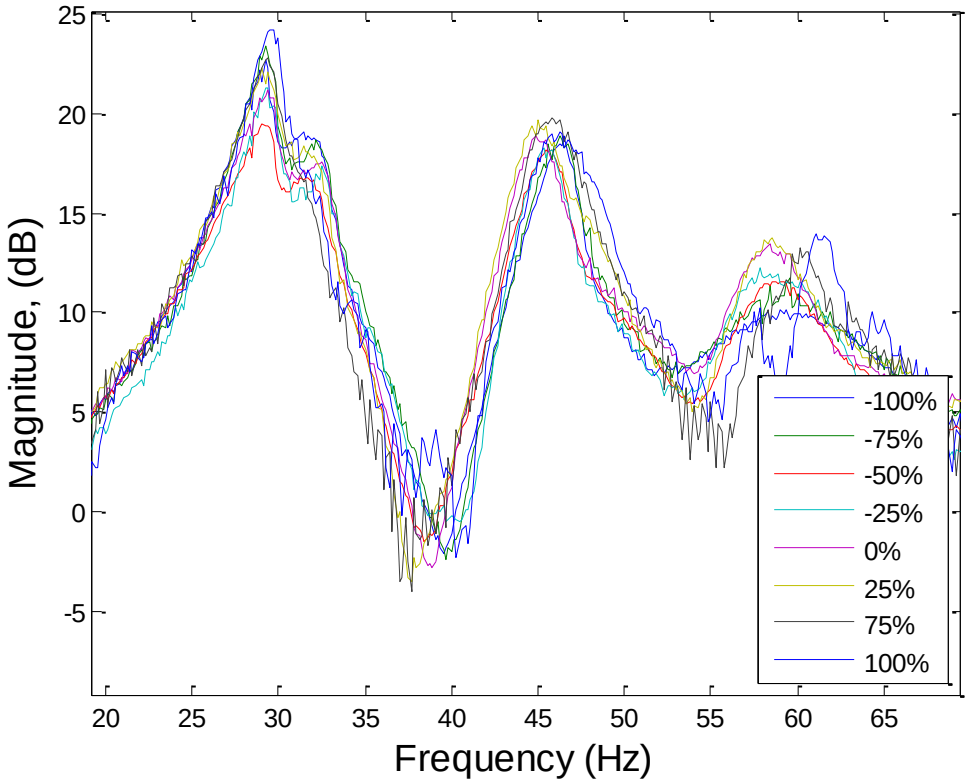

Figure 16: Frequency response function at various MFC actuation percentages

The actuated airfoil had a more interesting modal plot than the unactuated cases shown previously. The first resonance separates into two separate peaks that were not seen in the previous modal plots. The actuated MFC effectively stiffens the composite surfaces of the airfoil by adding mechanical strain to the trailing edge. As a result, the first resonance which was overly damped in the previous modal plots begins to show more detail in the mode shape at this frequency region. Another contributor that likely prevented the detection of these modes in the first two experiments was the location of the impulse. Impacts were implemented on the quarter chord which is effectively right on top of a node. Additional stiffness also shifts the second resonance from 45 Hz to 46.5 Hz. This modal plot is not as clean as the previous modal experiments due to added strain from the MFCs.

Figure 17 below shows the modes of vibration for the airfoil and the load cell standoff based on the previous plots. The upper rectangle represents the airfoil and the thin strip at the bottom represents the load cell standoff which is fixed to a U-joint at the very bottom. In these diagrams, the plus sign represents one direction of movement, the minus sign represents

movement in the opposite direction, and the capital letter "N" represents a nodal line (used to better describe some plots). The modal tests above resulted in the following modal shapes.

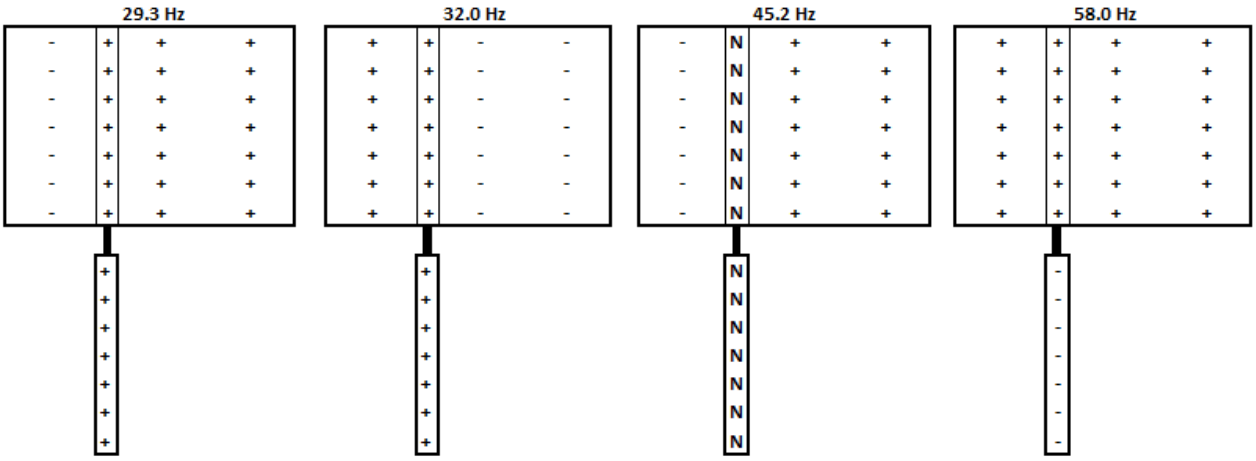

Figure 17: Unactuated Modes of vibration

The first and second mode only separate and shows up in the actuated case. In both unactuated modal tests, the first two modes are indistinguishable from one another and are viewed as a single mode that looks like Figure 18 below. Slight variations of the modal plots below may be due to the polynomial fit that was used to generate the surface. These mode shapes are further visualized with a simulation of surface displacement data collected during wind tunnel testing of the airfoil in Chapter 7 in order to further verify the mode shapes and to effectively connect empirical data to Chapter 3.

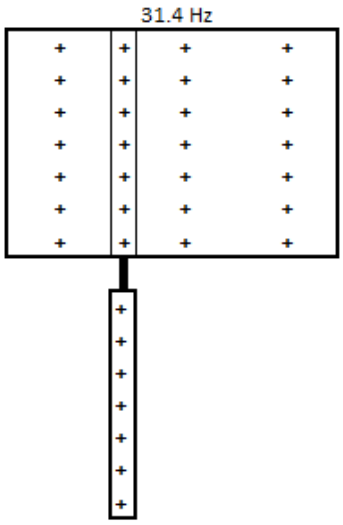

Figure 18: First mode for Unactuated Airfoil

In order to account for the dynamics of the load cell support system, an additional FRF test was conducted on the load cell response to impacts at the quarter chord of the airfoil. The support system and load cell response align closely with the LDV responses shown above.

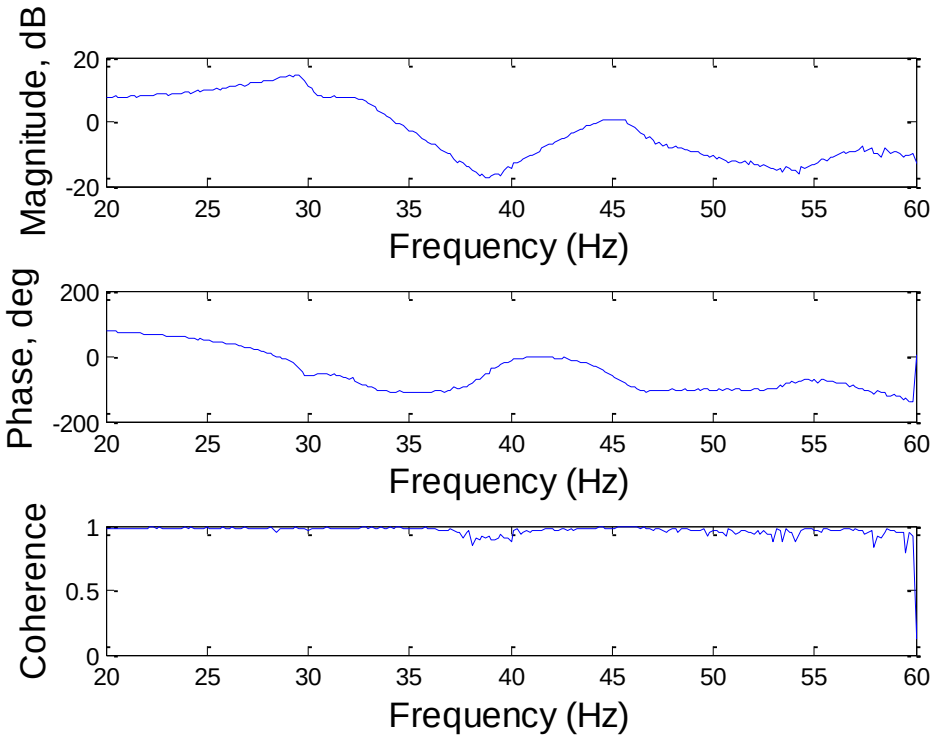

Figure 19: Load Cell Support System FRF

Chapter 6

Wind Tunnel Results

Modal testing of the airfoil and load cell apparatus provided insight into some of the occurrences that are recorded during wind tunnel testing. This chapter includes wind tunnel data and post processing used to produce meaningful results from that data. Wind tunnel lift data with both static and oscillatory MFC inputs was used to characterize aerodynamic loading and frequency response information for various airspeeds and actuation frequencies. Coefficients of lift plots are validated using a viscous XFOIL analysis of the airfoil at varying Reynolds numbers and angles of attack.

6.1 Static Test Results

This section presents wind tunnel test results from static actuation inputs. The primary motivation behind this section is to measure the effects of aerodynamic loading on the airfoil to gain a better expectation of performance out of MFC morphing airfoils.
Aerodynamic loading on an MFC airfoil can have a prominent effect on the airfoil trailing edge deflection and subsequently the lift that the airfoil can generate. Probst [5] mentioned these effects while comparing MFC airfoils to conventional servomechanisms for the purpose of UAV roll authority in fixed wing aircraft.

In order to measure the effect of aerodynamic loading on airfoil trailing edge deflection, the displacement of the airfoil trailing edge was measured at various airspeeds while the MFCs were actuated at a static 0%, +90% and -90% of their full actuation range. An initial support angle of 0 degrees was selected to keep far below the airfoil stall region when the airfoil actuated.

Prior to each experiment, the MFC's hysteresis was accounted for by actuating the airfoil fully +100% for the +90% trials and -100% for the -90% trials. It is important to note that the 0% actuation trials were conducted after the MFCs had been actuated to +100% so there may be some positive actuation bias in these results. Each of the actuation amplitude was tested at 0m/s,

9m/s, 13m/s and 17m/s. These air speeds were selected to align with previous experiments that Probst conducted on the same airfoil for the purpose of comparison. The Reynolds number associated with these airspeeds is presented below in Table 2.

Table 2: Reynolds Number of Airspeeds

Air Speed	Reynolds Number
9 m/s	7.3×10^4
13 m/s	1.1×10^5
17 m/s	1.4×10^5

The data collected was smoothed using a fourth order low pass Butterworth filter with a cutoff frequency of 60Hz to remove noise and produce meaningful figures. The unactuated airfoil has higher amplitude oscillations in trailing edge deflection than both of the actuated experiments. This can be partially attributed to a reduction in structural stiffness due to the absence of piezoelectric induced strain. Figure 20 shows the oscillations of an unactuated airfoil are larger in magnitude at intermediate airspeeds of 9 m/s and 13m/s.

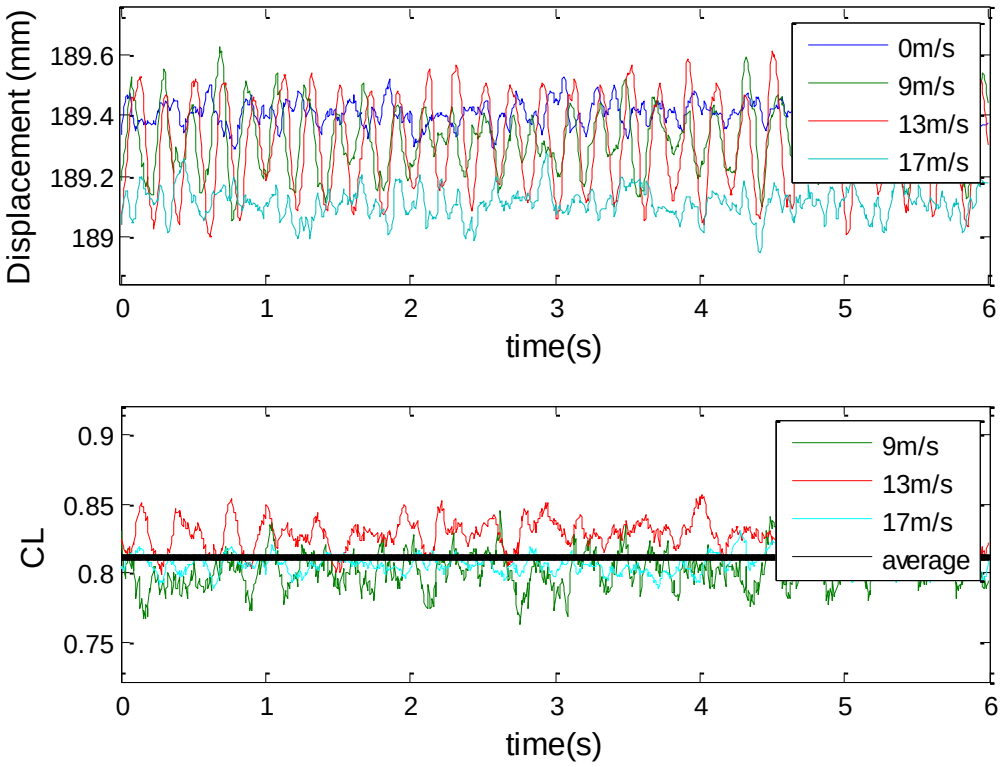

Figure 20: Unactuated deflection from aerodynamic loading (top) and coefficient of lift (bottom)

Oscillations of the trailing edge are nearly 41% larger with an intermediate airspeed of 13m/s in comparison to 17m/s. This is expectedly due to the particular frequency at which the trailing edge was oscillating. An FFT of the oscillating deflections shows the 9m/s and 13m/s airspeeds have a more pronounced 30Hz excitation of the trailing edge than the 17m/s airspeed. This particular frequency matches the resonance of the airfoil and load cell apparatus found in chapter 3. This fluttering phenomenon is characterized as a Limit Cycle Oscillation (LCO). LCOs result from a coupling between the sustained airflow and the aero elasticity of a structure [23] that excites the structure into oscillation. This form of flutter is limited by nonlinearities in the stiffness of the structure and does not continue to resonate until failure but the sustained oscillations are typically undesirable.

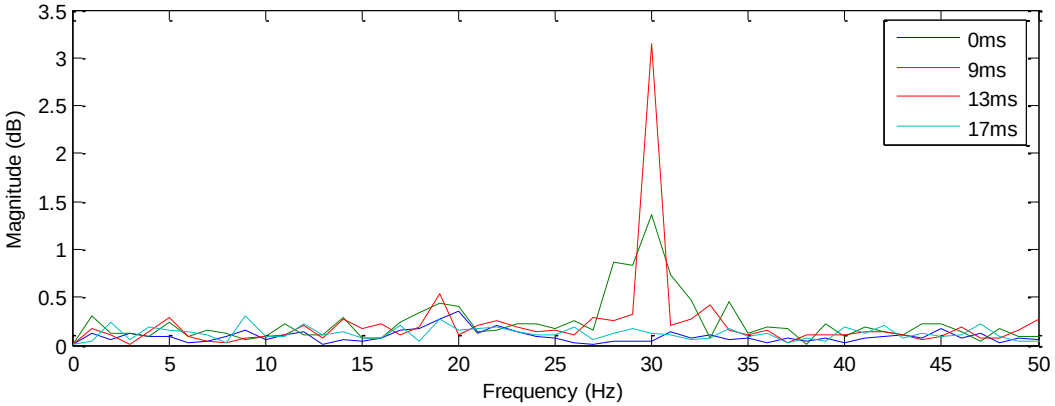

Figure 21: FFT of unactuated airfoil at various airspeeds

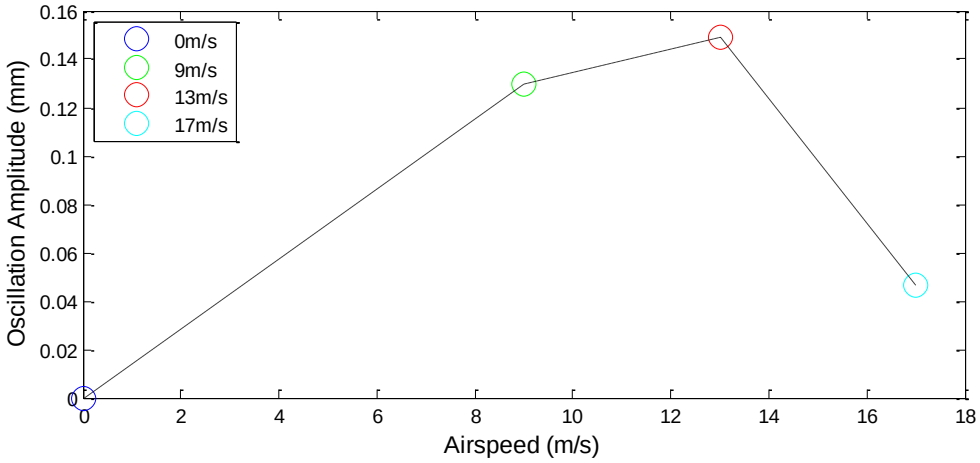

Figure 22: Trailing edge oscillation amplitude of unactuated airfoil at various airspeeds

Trailing edge displacement of the -90% actuated airfoils resulted in smaller trailing edge oscillations. Negative MFC inputs resulted in trailing edge deflections that were minimal in comparison to both the unactuated and the +90% actuated case. The amplitude of trailing edge oscillations with +90% and -90% actuation were too close to the sensor noise floor to conclude any results. Trailing edge deflection is the largest at +90% actuation due to the resulting high angle of attack from the camber inducing MFCs. The average trailing edge deflection from aerodynamic loading at 17m/s with +90% actuation in comparison to 0 m/s is 6.7 mm.

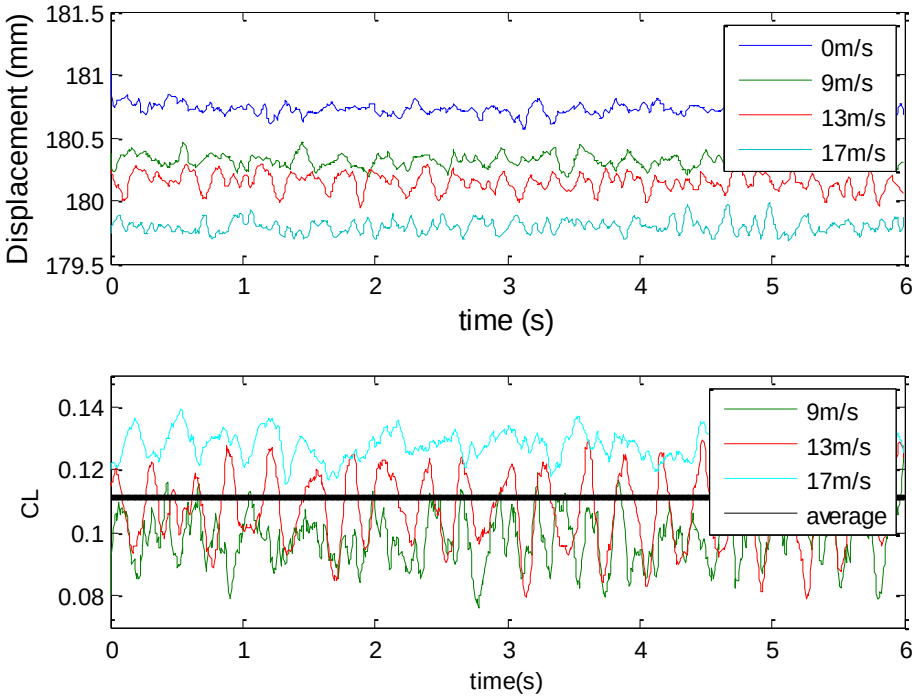

Figure 23: -90% Static airfoil trailing edge deflection from aerodynamic loading (top) and coefficient of lift (bottom)

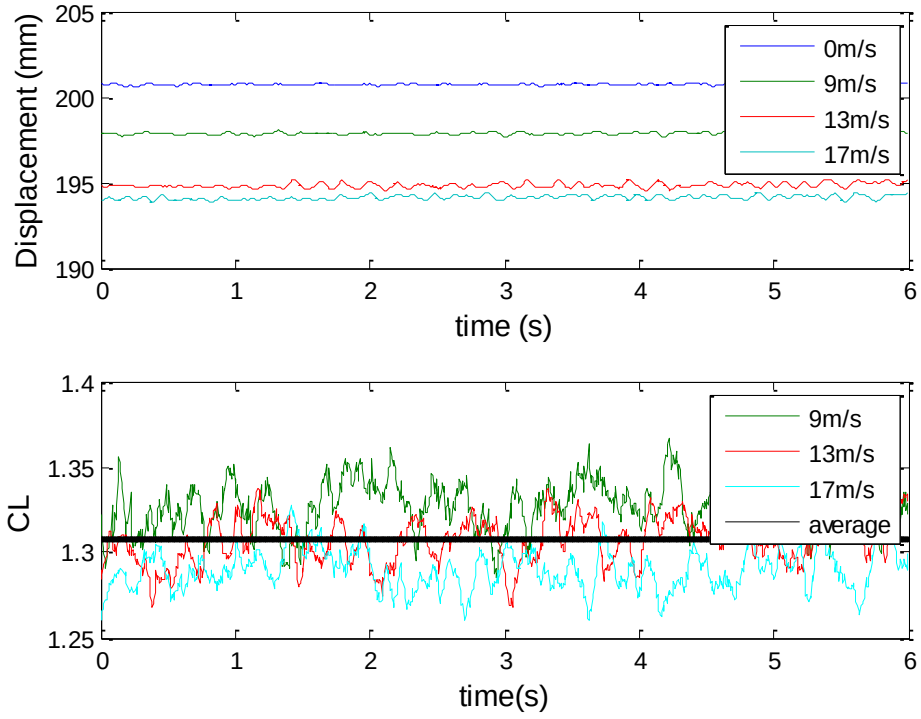

Figure 24: +90% Static airfoil deflection from aerodynamic loading

6.2 Static Airfoil Theoretical Results

Static experiments were validated using XFOIL, a subsonic airfoil development program written in FORTRAN that utilizes the panel method along with compressibility corrections for relatively accurate viscous or inviscid analysis [24]. XFOIL was driven using XFLR5 [25], a C++ translation with a more intuitive user interface that easily allows for airfoil coordinate modification. XFOIL boundary layer conditions are modified by forcing transition and specifying the amplitude ratio $N_{crit} = 9$. This variable of the e^N method corresponds to average turbulence levels found within a wind tunnel [26]. Results with Reynolds numbers ranging from $7x10^4 – 1.4x10^5$ produced an expected coefficient of lift that aligned closely with the experimental results. The XFOIL results for the coefficient of lift vs AOA with no additional camber added are shown below in Figure 25.

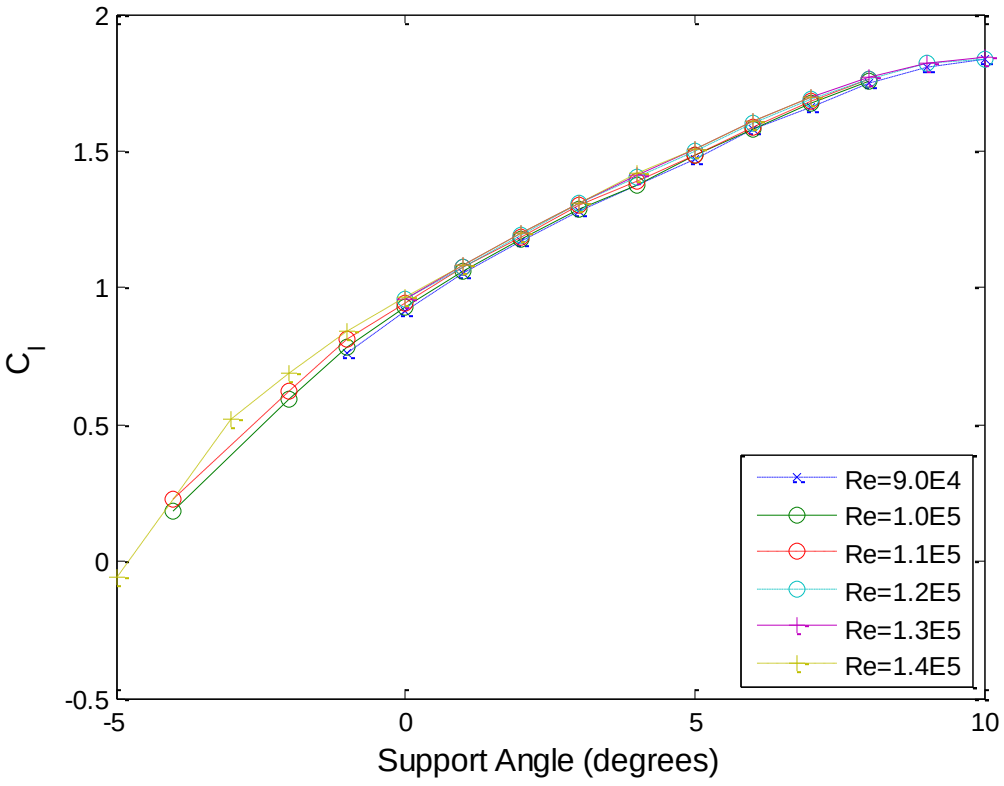

Figure 25: XFOIL C_L at various angles of attack with no additional camber

The AOA of zero degrees shown above is used for comparison to the unactuated airfoil with a support angle of zero degrees. XFOIL suggests the coefficient of lift will be approximately 0.9 for the airfoil at this AOA which is slightly higher than the average coefficient of lift measured in the experimental results. Theoretical unactuated coefficients of lift for the Selig 1210 airfoil align with low speed airfoil data collected by Selig [15]. Torsion about the load cell standoff is accounted for by measuring the trailing edge deflection and normalizing this measurement with the displacement of the quarter chord of the airfoil. This information used in addition to the streamline correction coefficient to correct for the angle of attack in each experiment. Measured coefficients of lift are compared to theoretical values for the coefficient of lift determined in XFOIL and summarized in the table below.

Table 3: Summary of C_L data for 0% Actuation Configuration

Actuation Percentage	Airspeed (m/s)	C_l Measured	C_l Theoretical	TE Displacement (mm)
0%	9	0.80	0.83	0.4
	13	0.83	0.86	0.4
	17	0.80	0.91	0.5

In order to validate the positively and negatively actuated airfoil results, the airfoil contour was modified in XFLIR5 to add or remove additional camber into the airfoil using the design toolbox. Inconsistencies in the airfoil geometry that prevented XFOIL from converging were resolved by manually adjusting certain airfoil coordinates to create a continuous airfoil shape by interpolation. Figure 26 shown below is an example of small inconsistencies that XFLIR5 can create that will prevent XFOIL from properly converging.

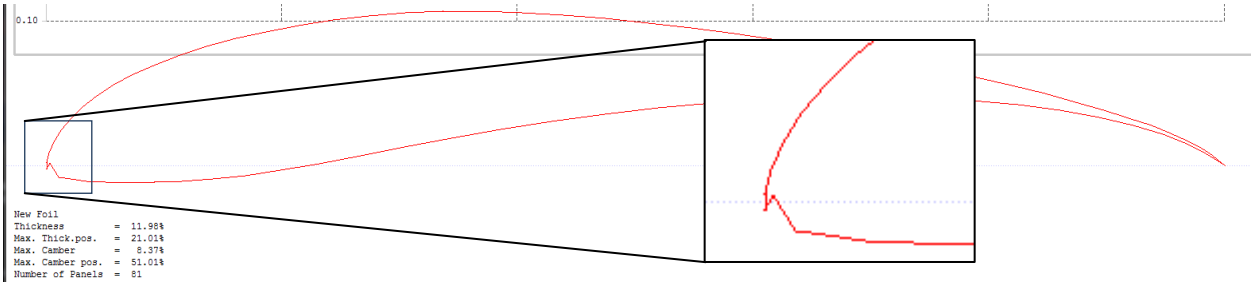

Figure 26: XFLIR5 geometric inconsistencies

After adjusting the camber line of the airfoil the angle of attack was shifted to accommodate the angle of attack that results from actuating the MFCs. XFLIR5 automatically adjusts the cambered airfoil to have zero AOA whereas during experimentation, the airfoil is fixed at the quarter chord and thus changes AOA with changes in the camber line. XFOIL results for the coefficient of lift vs angle of attack after adding and removing camber can be seen in Figure 27 and Figure 28 respectively.

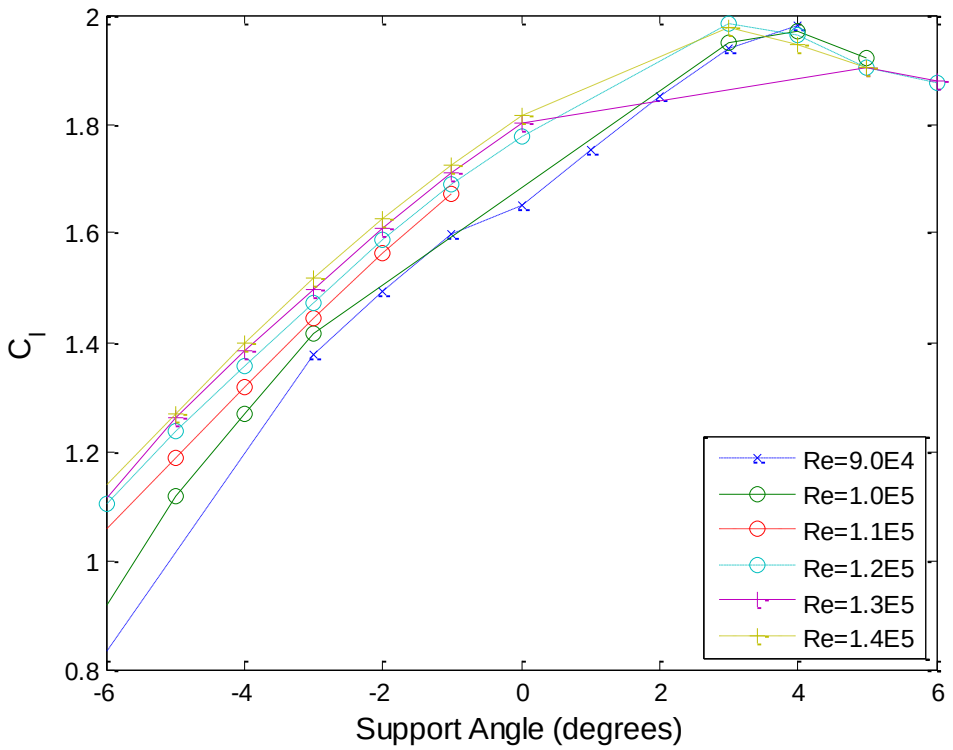

Figure 27: XFOIL C_l at various angles of attack with positive camber

In this positive camber, high lift configuration, the airfoil stalls at a shallower angle of attack in comparison to the unactuated airfoil. This occurs due to the higher lift configuration of the airfoil combined with an increase in angle of attack associated that results from additional camber to the trailing edge. A summary of measured coefficients of lift in comparison with theoretical values found in an XFOIL simulation can be seen below in Table 4.

Table 4: Summary of C_L data for +90% Actuation Configuration

Actuation Percentage	Airspeed (m/s)	C_l Measured	C_l Theoretical	TE Displacement (mm)
90%	9	1.33	1.61	3
	13	1.31	1.71	5
	17	1.29	1.74	6

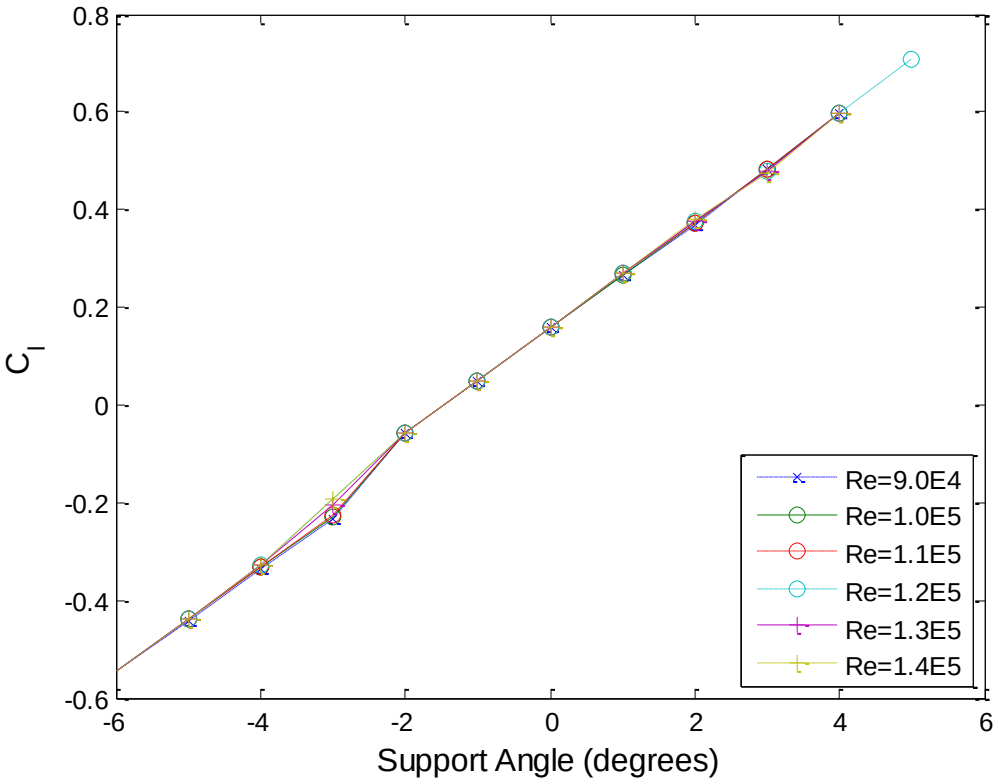

Figure 28: XFOIL C_L at various angles of attack with negative camber

Negative actuation inputs lead to a more linear coefficient of lift due to the more streamlined airfoil profile resulting from a reduction of camber. A summary of measured coefficients of lift in comparison to theoretical coefficients of lift determined by XFOIL with -100% actuation are shown below in Table 5. Underestimation of the coefficient of lift is due to elastic deformation of the trailing edge and variations in the airfoil profile that were not measured during the test like the maximum x-position for camber.

Table 5: Summary of C_l data for -90% Actuation

Actuation Percentage	Airspeed (m/s)	C_l Measured	C_l Theoretical	TE Displacement (mm)
-90%	9	0.09	0.09	0.4
	13	0.11	0.09	0.6
	17	0.12	0.09	1.0

Although useful as a tool for comparison of experimental studies to theoretical values, there are inherent limitations to the accurate representation of an experiment using XFOIL. XFOIL is a two dimensional airfoil analysis software that accounts for airfoil profile but the does not account for three dimensional flow characteristics that are present in wind tunnel experiments and the effects of three dimensional flow on the elasticity of the airfoil and load cell apparatus [27]. The panel method that XFOIL utilizes can accurately represent a limited amount of flow separation and as a result, higher angles of attack produce more error in relation to experimental results [28]. Elastic deformation of the airfoil will also cause inconsistencies in the airfoil geometry that vary the airfoil profile across the width of the airfoil. These variations in airfoil profile are not accounted for in XFOIL.

6.3 Dynamic Test Results

After measuring the effects of aerodynamic loading on the airfoil trailing edge deflection the dynamic response of the airfoil to an oscillatory input was measured. The purpose of these experiments was to measure the lift response to an oscillatory MFC input. After this information is collected, the phase difference between the MFC actuation input and the resulting displacement of the trailing edge as well as the phase difference from the MFC input signal to a resulting lift response is determined. This information is critical for implementation of MFCs in high speed control surface applications.

The frequencies selected for the MFC input signal reside between the resonances found in chapter 3. These were selected in order to avoid the resonant peaks and prevent over-attenuation of the trailing edge deflection due to bandwidth limitations of the drive circuitry. Control signals scaled the MFC actuation amplitude to 90% for all tests. This amplitude was selected because low actuation amplitude bandwidth data had already been measured in previous research. The bandwidth of higher actuation percentages better describes the lift authority that this MFC airfoil is capable of producing. Dynamic testing was conducted at the same airspeeds as the static testing section for the purpose of comparison. Lift responses shown exclude the initial half second of data collection to mitigate any transient effects of the MFCs beginning the oscillation cycle. Transient responses typically died out within the first 0.10 seconds.

This section is segregated by airspeed. FRF information is discussed for each frequency after the lift data and FFT are presented. All lift data sets were filtered using a second order Butterworth filter with a 60 Hz cutoff frequency to remove noise. The FFT was computed from the original unfiltered lift signal to preserve all frequency data. The lift data shown below in Figure 29 was measured without any airspeed and used as a control to compare all airspeeds tested. Note that this set of data is not actually lift but instead represents forces measured solely due to the inertial oscillations of the airfoil trailing edge. Lift data was normalized by subtracting the inertial response data from each of the lift data sets.

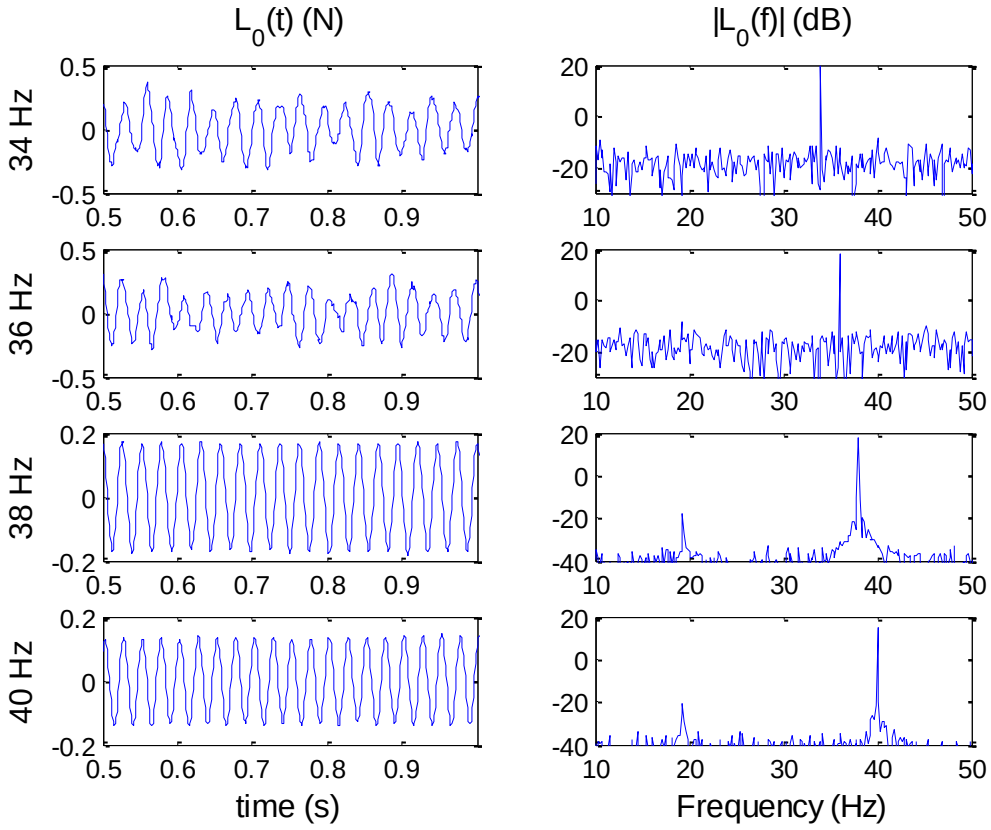

Figure 29: Inertial Response from 34-40Hz at V=0 m/s

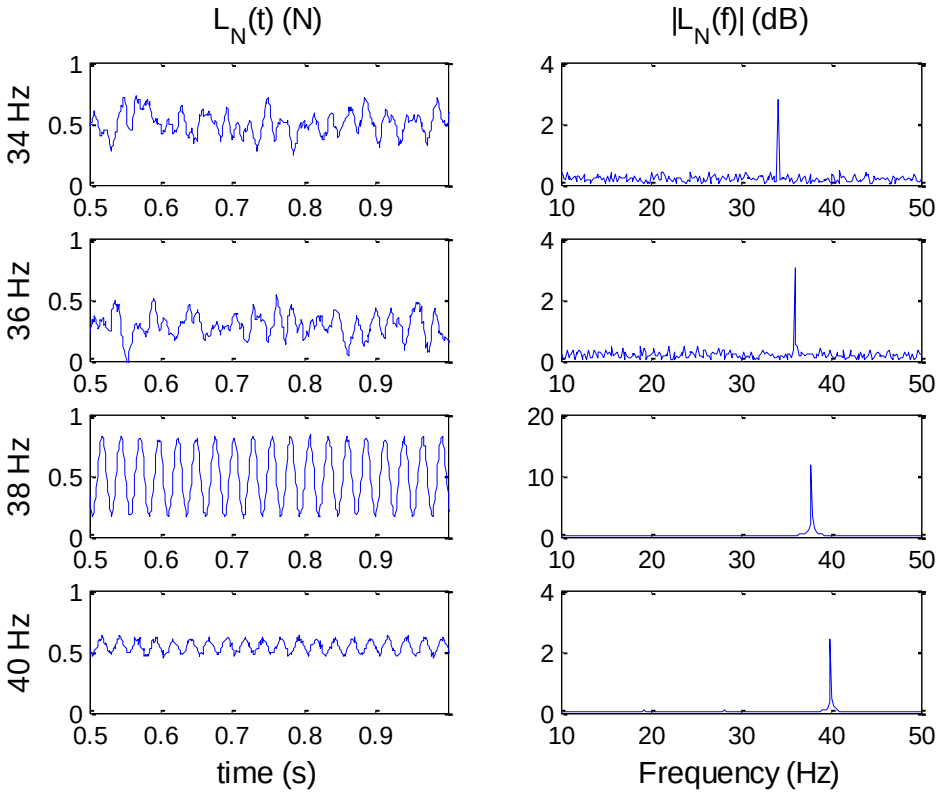

Figure 30: Normalized Lift Response from 34-40Hz at V=9 m/s

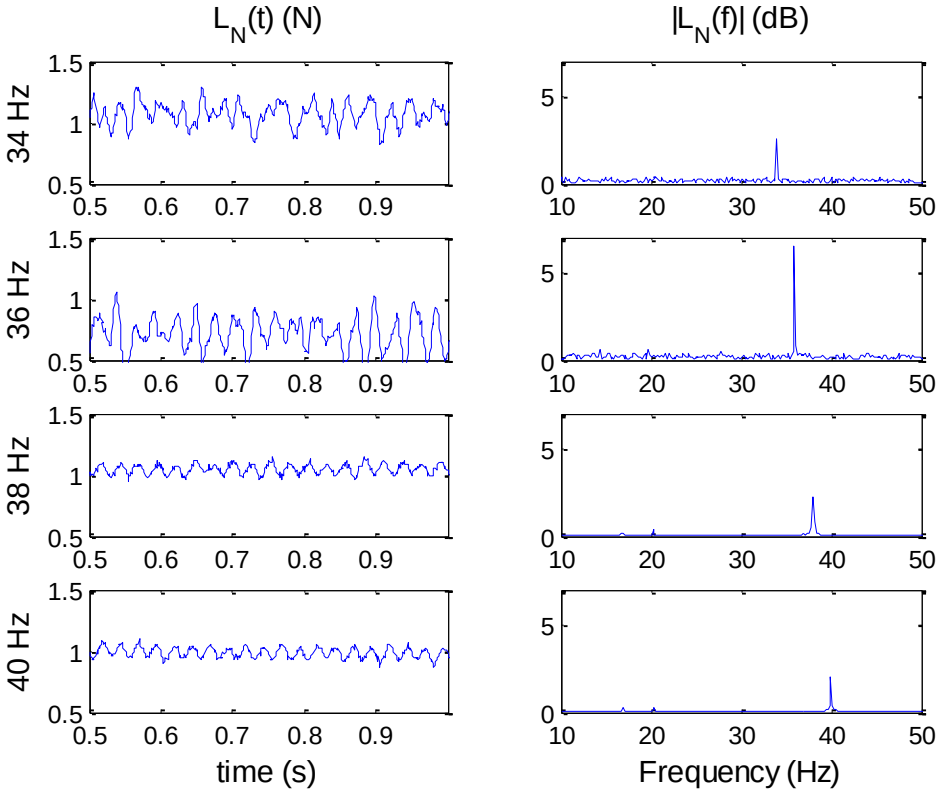

Figure 31: Normalized Lift Response from 34-40Hz at V=13 m/s

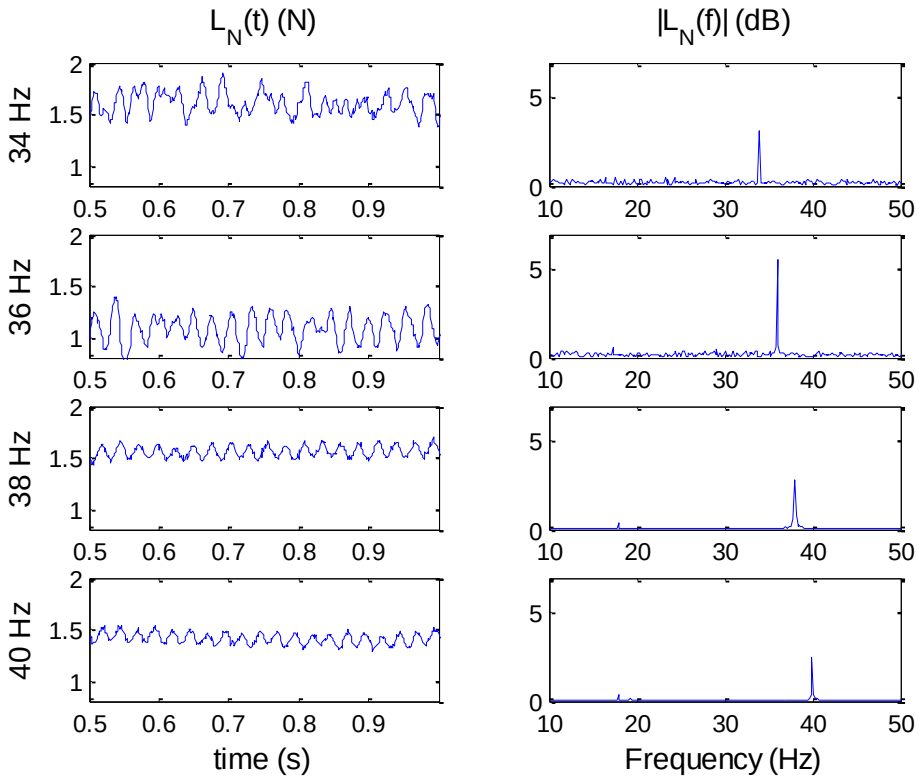

Figure 32: Normalized Lift Response from 34-40Hz at V=17 m/s

As the MFC input frequency increases there is a significant reduction in the oscillation amplitude of the lift response generated by the airfoil. The spectrum of the lift signal was computed to verify that the frequency content of the lift signal has a dominant component that matches the frequency from the MFC input signal. The spectrum of the lift data with airspeed is smaller in magnitude than the magnitude of the load cell data recorded without airspeed because oscillations are seemingly suppressed by the lift force that is pulling from the top surface of the airfoil. Greater airspeed increases the natural frequency of the airfoil due to the inherent stiffening element that results from airspeed. The magnitude of the FFT includes both the force generated by airfoil lift and the inertial component of the airfoil oscillating due to the mass of the MFC actuators, composite surface and carbon fiber trailing edge stiffener. The DC offset above represents the nominal lift generated by the airfoil at given airspeed. The inertial component expectedly becomes more prominent as the MFC actuation frequency approaches the 30 Hz resonant frequency found in chapter three.

In order to account for the inertial forces of the airfoil, the data recorded without any air speed is used to normalize the lift results produced with air speed included. The nominal lift force increases as expected with higher air speeds.

After determining the normalized lift component at each airspeed, the lag of the lift response from an input signal to the MFCs was computed. This information is summarized below both in angular units (degrees) and time (milliseconds). The lag in time is based off of the MFC input signal frequency. Complete FRF plots after normalization including magnitude, phase and coherence can be seen in section A6 and A7 of the appendix.

Table 6: Phase lag and time delay between MFC input signal and Lift response

degrees (ms)	**Frequency (Hz)**			
Airspeed (m/s)	**34**	**36**	**38**	**40**
9	31.3° (2.56)	43.1 ° (3.32)	84.9 ° (6.21)	117.1 ° (8.13)
13	30.0 ° (2.45)	47.1 ° (3.63)	102.6 ° (7.50)	82.9 ° (5.76)
17	28.0 ° (2.29)	51.5 ° (3.97)	72.5 ° (5.30)	96.5 ° (6.70)

Among the data collected, there is a notable difference in the magnitude of the airfoil trailing edge deflection for higher frequency oscillations. This is apparent in both Figure 29 and Figure 30 because the amplitudes of oscillation are reduced. This difference can be attributed to the lag in trailing edge displacement response to an actuation signal.

Bandwidth limitations in the bipolar circuit divider were determined after identifying that the displacement of the trailing edge was not reaching the same values as the static tests from the previous section. The driver circuit utilizes bleed resistors with significant resistance that allows the capacitive nature of the MFCs to discharge after the sinusoidal signal reaches a maximum or minimum value. The high voltage required to drive an MFC needs to dissipate through large resistors to prevent current spikes that could be potentially harmful to the circuitry. These resistors also need to be large in value due to their placement within the circuit. Since these resistors bridge the input directly to ground, a lower value would leak high currents and would

greatly reduce the circuit's efficiency. A schematic of this circuit can be seen below in Figure 33.

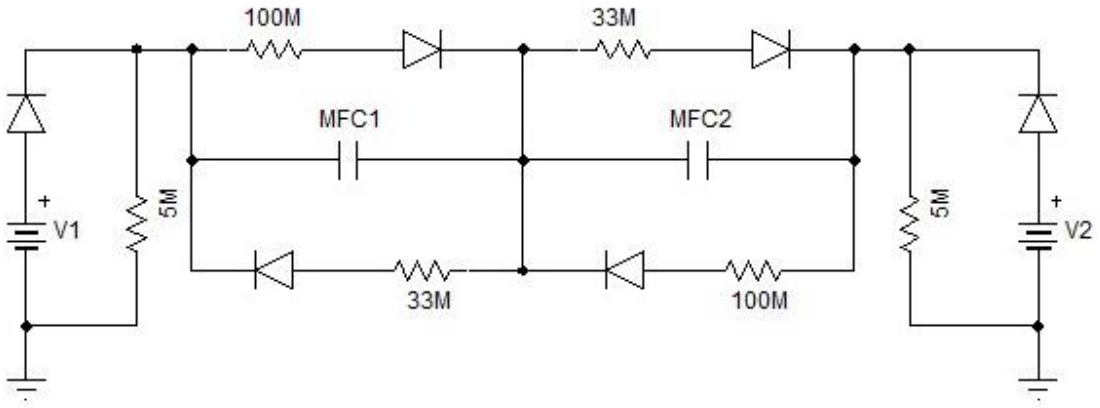

Figure 33: Asymmetric MFC Voltage Divider, O. Bilgen, "Aerodynamic and Electromechanical Design, Modeling and Implementation of Piezocomposite Airfoils," Virginia Tech, Blacksburg, 2010. Used with permission, 2014

Chapter 7

Airfoil Surface Model

This chapter explains how airfoil surface displacements measured during dynamic wind tunnel testing can be used to generate a cost effective empirical model of the airfoil surface contour. This could potentially be used for validating parametric models and to improve the accuracy of the geometric models used in vortex lattice simulations by including small dynamic surface deformations that are otherwise assumed to be nonexistent.

7.1 Surface Modeling Method and Assumptions

Surface displacement data is used to generate a 2D model of changes in airfoil contour during a wind tunnel test. Unactuated coordinates for the upper and lower airfoil surfaces were obtained from the UIUC Applied Aerodynamics Airfoil Coordinate Database [29]. In order to create the initial surface model, the airfoil was broken up between the upper MFC surface aft of the D-box, the lower wiper surface, and the leading edge D-box itself. Since the leading edge is constructed from basswood, it was assumed to be rigid for this model and only rigid body translation and pitch were considered for this section of the airfoil.

In order to model the fiberglass/MFC surface of the airfoil, the surface displacements were measured at various points along the airfoil span using a laser displacement sensor during oscillatory experiments. Potential phase differences in each experiment were accounted for by utilizing the MFC input signal as a clock reference. Data sets were shifted so that the phase of the MFC input signal from each experiment was aligned. Displacement data was smoothed using a fourth order low pass Butterworth filter with a 60 Hz cutoff frequency. The profile of the trailing edge MFC surface was created using a third order polynomial fit for each set of recorded displacement data. This polynomial is reconstructed for each data set to reflect the current profile of the airfoil at each sample instance. A third order polynomial was selected as a

compromise between accuracy and computation time. The polynomial estimate provides a reasonable fit to the unactuated airfoil with a coefficient of determination (R^2) value of 0.99.

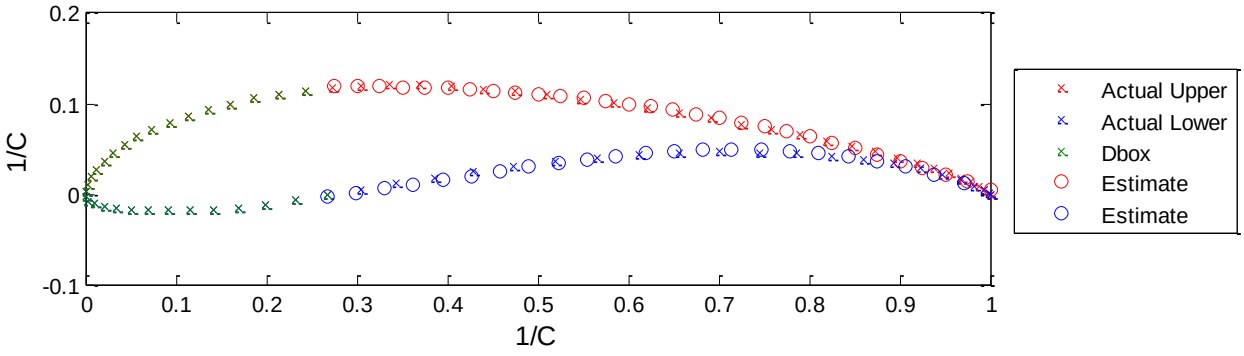

Figure 34: Segregation of airfoil profile for generating surfaces

Displacement of the lower airfoil surface was not measured in this research and assumed to have a constant distance from corresponding chordwise points on the upper surface. The lower profile could easily be generated using the same method explained above for the upper surface in order to improve the accuracy of this geometric model.

Since airfoil data was only collected spanning the airfoil chord, it was superimposed to create a three dimensional model by assembling multiple copies of the profile data into an array. This array can be assembled from data measured normal to the chord direction to further improve the accuracy of the model but will consequently include more information relating to the load cell apparatus dynamics.

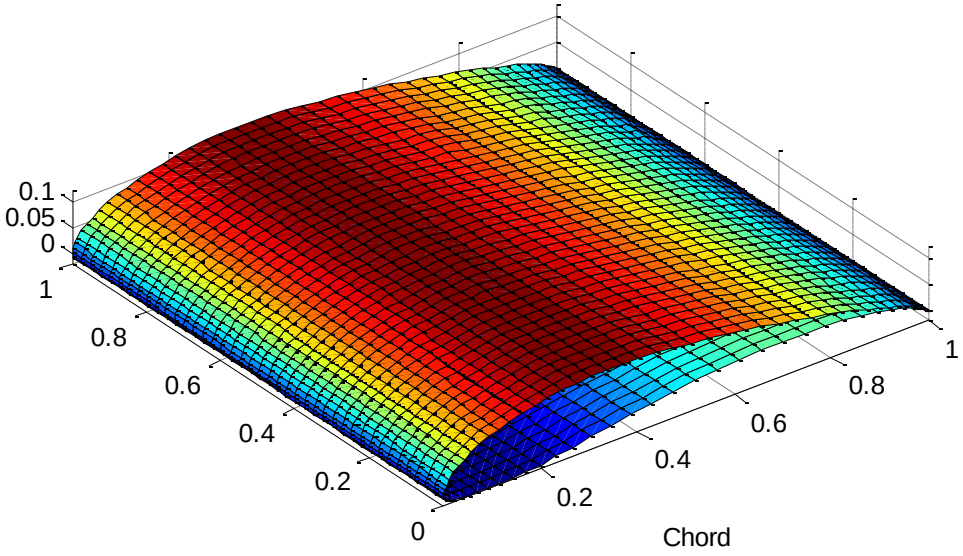

Figure 35: Surface contour model of unactuated Selig S1210

After segmenting the airfoil into separate sections and reassembling coordinates to create the morphing airfoil surface, a small gap existed between the leading edge and the flexible surfaces. This gap was determined to be due to a difference in pitch between the leading edge and trailing edge of the airfoil. In order to account for this discontinuity, angular variations of the leading edge were measured using the following equations:

$$\theta = \tan^{-1}\left(\frac{z_2(t) - z_1(t)}{x_2 - x_1}\right) - \tan^{-1}\left(\frac{z_2(0) - z_1(0)}{x_2 - x_1}\right) \tag{E7.1}$$

$$R_{xz} = \begin{bmatrix} \cos(\theta) & -\sin(\theta) \\ \sin(\theta) & \cos(\theta) \end{bmatrix} \tag{E7.2}$$

$$\begin{bmatrix} x_r \\ z_r \end{bmatrix} = [R_{xz}] \begin{bmatrix} x(t) - x_{qc} \\ z(t) - z_{qc} \end{bmatrix} + \begin{bmatrix} x_{qc} \\ z_{qc} \end{bmatrix} \tag{E7.3}$$

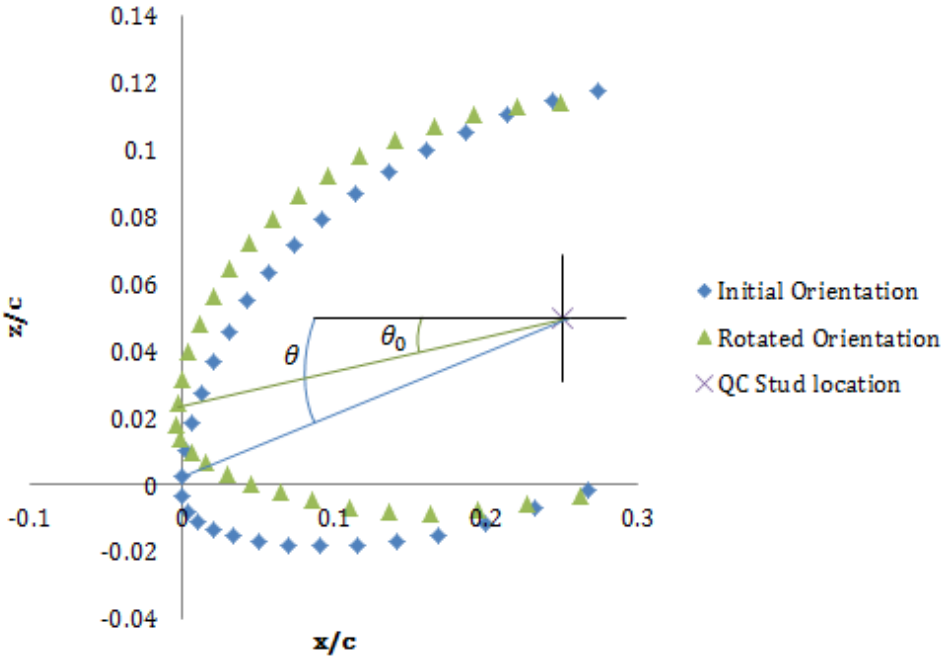

Figure 36: Surface Model Angle of Attack

Where z_1 and z_2 are displacement measurements at two measurement locations on the leading edge and x_1 and x_2 are the x-coordinates associated with these measurements. The x and z-coordinates of the trailing edge were translated so that the quarter chord of the airfoil was at the origin. This ensured the leading edge coordinates were rotated about the quarter chord rather than the current origin. A rotation matrix was then applied to the leading edge coordinates for each data set prior to building each surface. After rotating the leading edge, the quarter chord was translated back into position. The resulting surface model based on measured data at various time steps can be seen below in Figure 37.

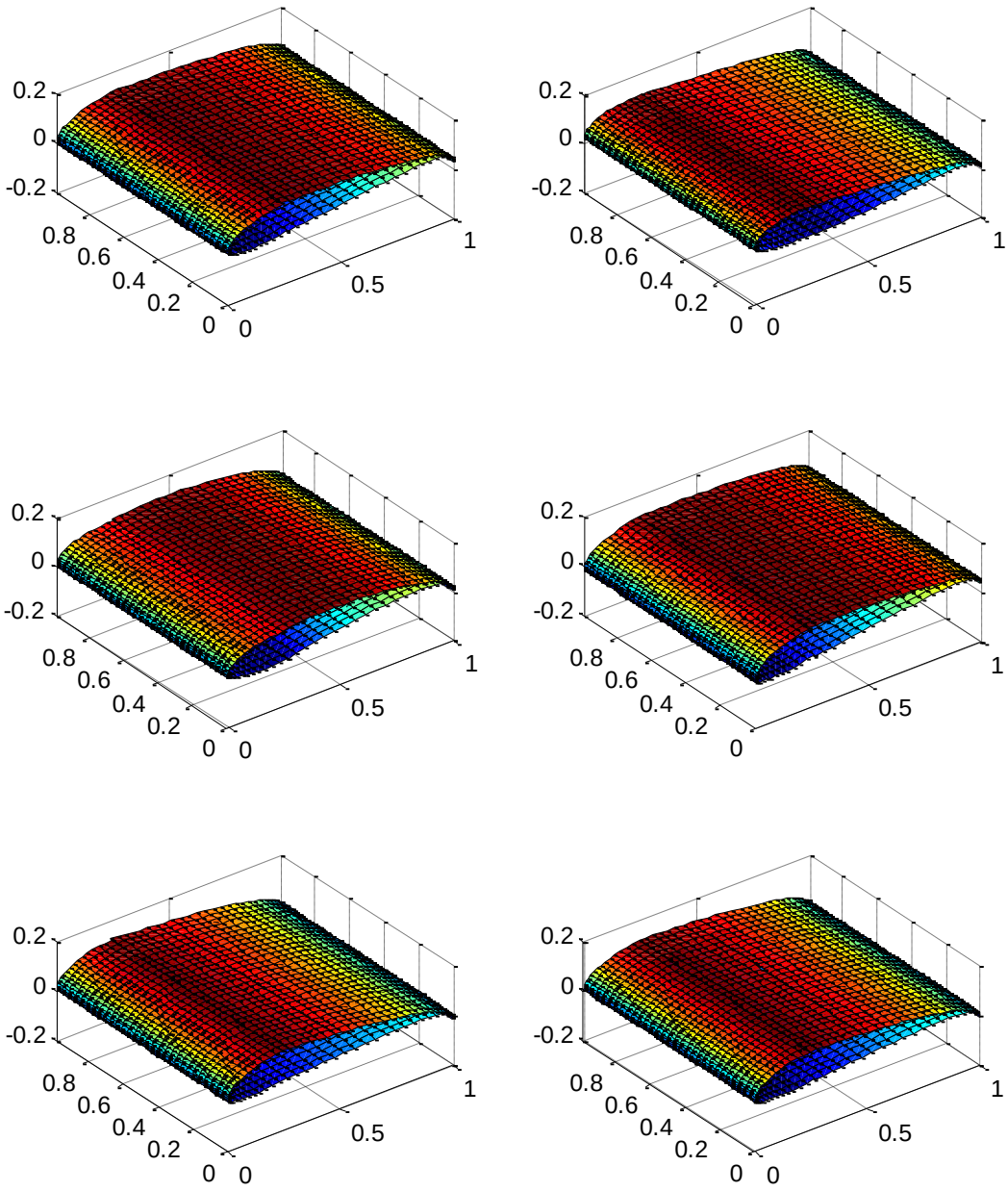

Figure 37: Snapshots of Airfoil Geometric Simulation

Chapter 8
Conclusion

8.1 Summary

This research presents experimental results of oscillatory lift generated using MFC morphing airfoils for the purpose of evaluating the use of Macro-Fiber Composites as an oscillatory lift control mechanism. Modal analysis of the airfoil and load cell structure highlighted resonant frequencies and mode shapes of the airfoil. This provided insight as to what vibratory phenomena is to be expected during wind tunnel testing due to the load cell and airfoil structure. The effect of aerodynamic loading on trailing edge deflection with high MFC actuation percentages and without actuation was measured at various airspeeds. Flutter characteristics from aerodynamic loading were analyzed and the magnitudes of oscillation were shown to vary significantly with airspeed. Deviations in the coefficient of lift from expected values due to aerodynamic loading were measured up to 17 m/s.

Bandwidth limitations of the current amplifier, driver circuitry, and MFC structure were discovered and shown to have a significant impact on the resulting amplitude of a bimorph MFC configuration. Transfer functions between the input signal and lift response are used to account for inertial forces generated by the oscillating airfoil and to extract magnitude and phase information at various airspeeds and input frequencies. Lag in the lift response from the MFC input signal was recorded at various air speeds and actuation frequencies for high actuation inputs. Airfoil surface displacement was measured at various points on the airfoil during oscillatory testing and used to create a geometric model of changes in the airfoil contour during wind tunnel testing.

The bandwidth performance of MFCs as an oscillatory lift mechanism is limited by both the structure that the MFCs are bonded to and the amplifier/divider circuitry used to supply the high voltage requirements. Aerodynamic and mechanical systems utilizing this technology as an actuator would benefit from feedback control to compensate for both hysteresis and aerodynamic loading.

8.2 Recommendations for Future Work

This research focused on analyzing experimental results of oscillatory lift in a specific airfoil configuration with one type of MFC. There is still work to be done in determining characteristics of a broader selection of these actuators. The relatively low cost of these actuators has given way to custom MFC configurations that can be made to order [1]. Comparison of the performance characteristics with custom MFC shapes versus the standard actuator footprint is not yet documented. Experimentation on the effects of laminate adhesives on the performance characteristics of MFCs would be another interesting analysis that could help characterize the effects of different bonding agents. Testing of symmetric airfoils with MFCs on the upper and lower surface could provide more actuator authority in aerodynamic applications. The ability to morph a symmetric airfoil to produce an asymmetric contour in either direction could benefit UAVs that fly inverted often.

Computational fluid dynamics simulations and smoke wire visualization of MFCs would help to further characterization of limit cycle oscillations that are a trending phenomenon in MFC wind tunnel testing. Effects on of oscillating camber on vortex formation could shed light on optimum oscillatory frequencies for specific airfoil shapes. Investigation of leading edge and trailing edge vortices could provide more insight into aerodynamic coupling between the structure and wake. Active control to dampen limit cycle oscillations would also make for another exciting research topic. This investigation into higher harmonic control is currently being studied by many other researchers.

The wind tunnel could be updated to include a measurement system for the airfoil pitching moment that results from a varying center of pressure when the airfoil morphs. This measurement system would provide more detailed expectations for resulting pitch when MFC control surfaces are actuated.

Bibliography

[1] "smart-materials.com," Smart Material, [Online]. Available: http://www.smart-material.com/MFC-product-main.html. [Accessed 2014].

[2] W. Wilkie, D. Inman, J. High and R. B. Willams, "Recent Developments in NASA Piezocomposite Actuator Technology," in *9th International Conference on New Actuators; 14-15 Jun. 2004; Breman; Germany*, 2004.

[3] O. Bilgen, "Aerodynamic and Electromechanical Design, Modeling and Implementation of Piezocomposite Airfoils," Virginia Tech, Blacksburg, 2010.

[4] E. Gustafson, "Design, Simulation, and Wind Tunnel Verification of a Morphing Airfoil," Virginia Tech, Blacksburg, Va, 2011.

[5] T. Probst, "Evaluating the Aerodynamic Performance of MFC-Actuated Morphing Wings to Control a Small UAV," Virginia Tech, Blacksburg, VA, 2012.

[6] D.-K. Kim and J.-H. Han, "Smart Flapping Wing Using Macro-Fiber Composite Actuators," *SPIE 13th Annual Symposium Smart Structures and Materials*, 2006.

[7] R. Duffy, J. Dubben, J. Nickerson and J. Colasante, "A Theoretical and Experimental Study of the Snap-Through Airfoil and its Potential as a Higher Harmonic Control Device," *AIAA 26th Aerospace Sciences Meeting*, no. AA-88-0668, 1988.

[8] N. Pern and J. Jacob, "Wake Vortex Mitigation Using Adaptive Airfoils: The Piezoelectric Arc Airfoil," *37th AIAA Aerospace Sciences Meeting and Exhibit*, no. 99-0524, 1999.

[9] D. Munday and J. Jacob, "Active Control of Separation on Wing with Oscillating Camber," *AIAA Aerospace Sciences Meeting and Exhibit*, no. AIAA-2001-0293, 2001.

[10] J. Clement, "Bench-Top Characterization of an Active Rotor Blade Flap System Incorporating C-Block Actuators," *AIAA*, vol. 98, pp. 2857-2869, 1998.

[11] J. Garcia, "Active Helicopter Rotor Control Using Blade-Mounted Actuators," Massachusetts Institute of Technology, Cambridge, 1994.

[12] F. Straub and D. Merkley, "Design of a Smart Material Actuator for Rotor Control," *Smart Material Structures*, pp. 223-234, 1997.

[13] T. Mueller, "Aerodynamic Measurements at Low Reynolds Numbers for Fixed Wing Micro-Air Vehicles," Department of Aerospace and Mechanical Engineering, University of Notre Dame, Notre Dame, IN, 1999.

[14] R. W. a. P. A. Barlow J.B., Low-Speed Wind Tunnel Testing, John Wiley and Sons 3rd ed., 1999.

[15] M. a. G. J. a. B. A. a. G. P. Selig, "Summary of Low-Speed Airfoil Data," SolarTech Publications, Virginia Beach, 1995.

[16] "Clarkson University," [Online]. Available: http://people.clarkson.edu/~pmarzocc/AE429/AE-429-4.pdf. [Accessed September 2014].

[17] O. J. Ohanian, "Piezoelectric Composite Morphing Control Surfaces for Unmanned Aerial

Vehicles," *Sensors and Smart Structures Technologies for Civil, Mechanical, and Aerospace Systems,* vol. 7981, 2011.

[18] S.-W. L. T.-Y. W. T.-J. Yeh, "Modeling and Identification of Hysteresis in Piezoelectric Actuators," *Journal of Dynamic Systems, Measurement, and Control,* vol. 128, June 2006.

[19] Noliac, "www.noliac.com'Material_characteristics," 2011. [Online]. Available: http://www.noliac.com/Material_characteristics_-143.aspx. [Accessed 20 July 2014].

[20] J. H. Schafer J, "Compensation of Hysteresis in Solid-State Actuators," *Sensors and Actuators,* pp. 97-102, 1995.

[21] H. J. K. Kuhnen, "Compensation of the Creep and Hysteresis Effects of Piezoelectric Actuators with Inverse Systems," University of Saarland, Saarbrucken, Germany.

[22] C. Visone, "Hysteresis Modelling and Compensation for Smart Sensors and Actuators," *International Workshop on Multi-Rate Processes and Hysteresis; Journal of Physics: Conference Series 138,* vol. 138, 2008.

[23] P. Mayuresh, "Limit Cycle Oscillations of Aircraft due to Flutter-Induced Drag," *AIAA Structures, Structural Dynamics, and Materials Conference,* vol. 43, 2002.

[24] M. a. Y. H. Drela, "XFOIL Subsonic Airfoil Development System (Version 6.99)," MIT, Dec 2013. [Online]. Available: http://web.mit.edu/drela/Public/web/xfoil/. [Accessed 29 August 2014].

[25] "xflr5.com," 1 February 2014. [Online]. Available: http://www.xflr5.com/ReleaseNotes.htm. [Accessed June 2014].

[26] M. Drela, "XFOIL Subsonic Airfoil Develpment System," [Online]. Available: http://web.mit.edu/drela/Public/web/xfoil/. [Accessed September 2014].

[27] D. Boon, "Application of Uncertainty Quantification to a Fluid-Structure Interaction Experiment - Providing Accurate Insight in Uncertain Phenomena," Delft University of Technology, Netherlands, 2011.

[28] T. Speer, "Aerodynamics Of Teardrop Wingmasts," Des Moines, Washington.

[29] U. A. A. G. -. D. o. A. Engineering, "UIUC Airfoil Coordinates Database," [Online]. Available: http://aerospace.illinois.edu/m-selig/ads/coord_database.html. [Accessed 12 03 2014].

[30] P. Cantrell, "The Helicopter Aviation Home Page," [Online]. Available: http://www.copters.com/helicopter.html. [Accessed 27 April 2014].

[31] P. Ge and M. Jouaneh, "Tracking Control of a Piezoceramic Actuator," *IEEE Trans on Control sys. Tech.,* pp. 209-216, 1996.

[32] G. D. a. D. Balmford, Bramwell's Helicopter Dynamics Second Edition, A.R.S. Bramwell and AIAA, 2001.

[33] L. T. G. S. G. T. T. N. Burner A.W., "Aeroelastic Deformation Measurements of Flap, Gap, and Overhang on a Semispan Model," *Journal of Aircraft,* vol. 38, no. 6, pp. 1147-1154, 2001.

[34] R. Bielawa, Rotary Wing Structural Dynamics and Aeroelasticity, Salem: American Institute of Aeronautics and Astronautics, 1992.

[35] M. a. W. K. Wilber, "Active-Twist Rotor Control Applications for UAVs," *nasa.gov,* 2004.

[36] J. Pope A. and Harper, Low Speed Wind Tunnel Testing, New York: Wiley and Sons, 1966.

[37] I. Ross, "Wind Tunnel Blockage Corrections: An Application to Vertical-Axis Wind Turbines," University of Dayton, Dayton, Ohio, 2012.

Appendix

Load Cell Calibration

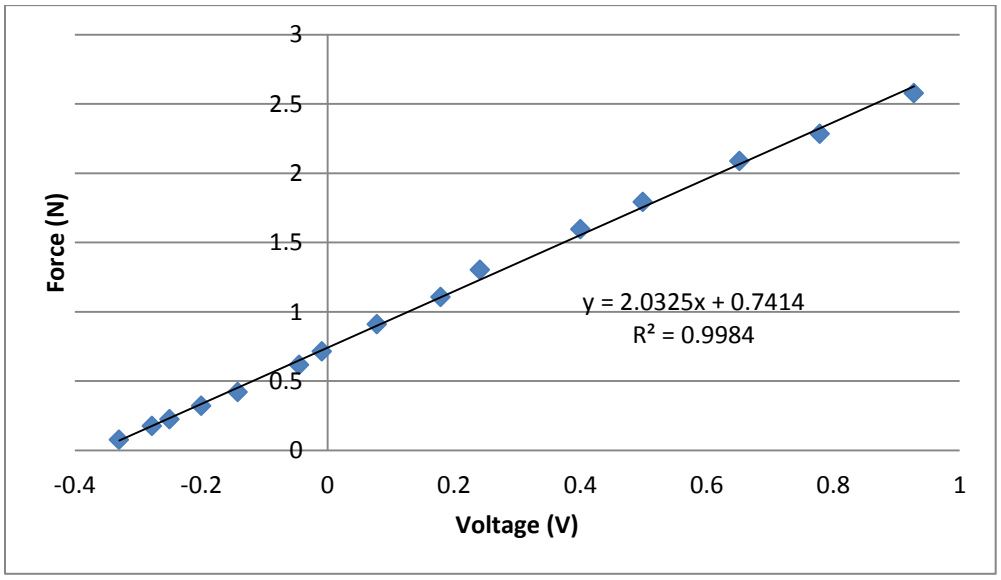

Figure 38: Lift Load Cell Calibration Curve

Laser Displacement Calibration

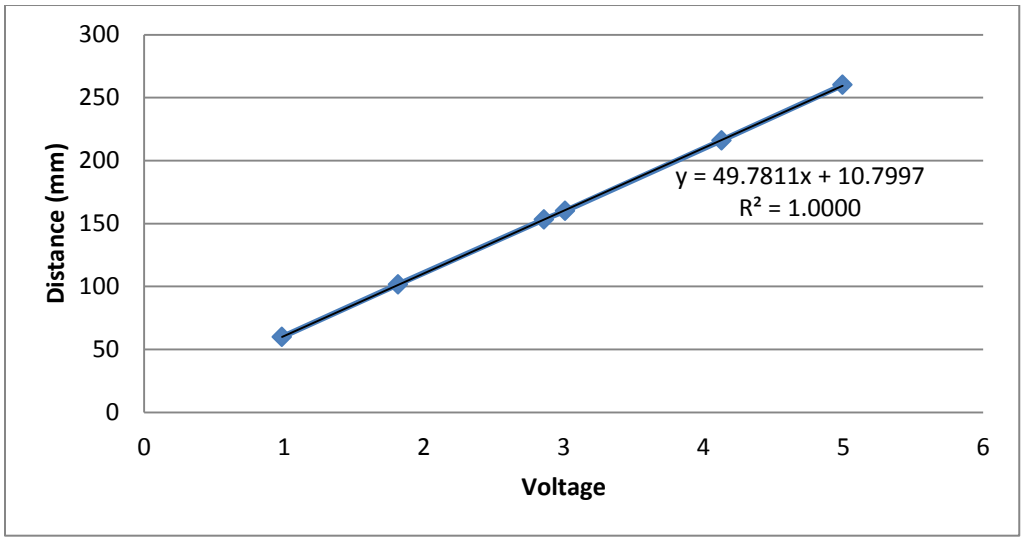

Figure 39: OptoNCDT ILD 1800-200 Calibration

Air Speed Stability

Table 7: Standard deviation of various airspeeds used during experiments

Air speed (m/s)	σ_1	σ_2	σ_3	Average Std.
9	0.1936	0.1919	0.1762	0.1872
13	0.1523	0.1543	0.1451	0.1506
17	0.1310	0.1297	0.1281	0.1296

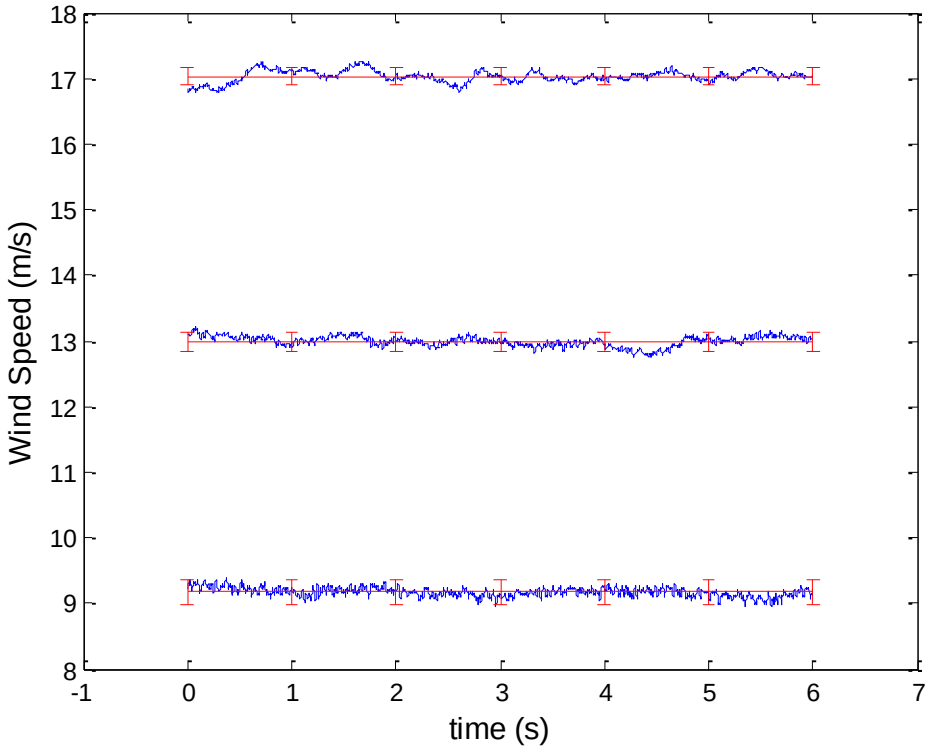

Figure 40: Wind Speed stability plot with error bars representing the averaged standard deviation

Modal Test Coherence Plots

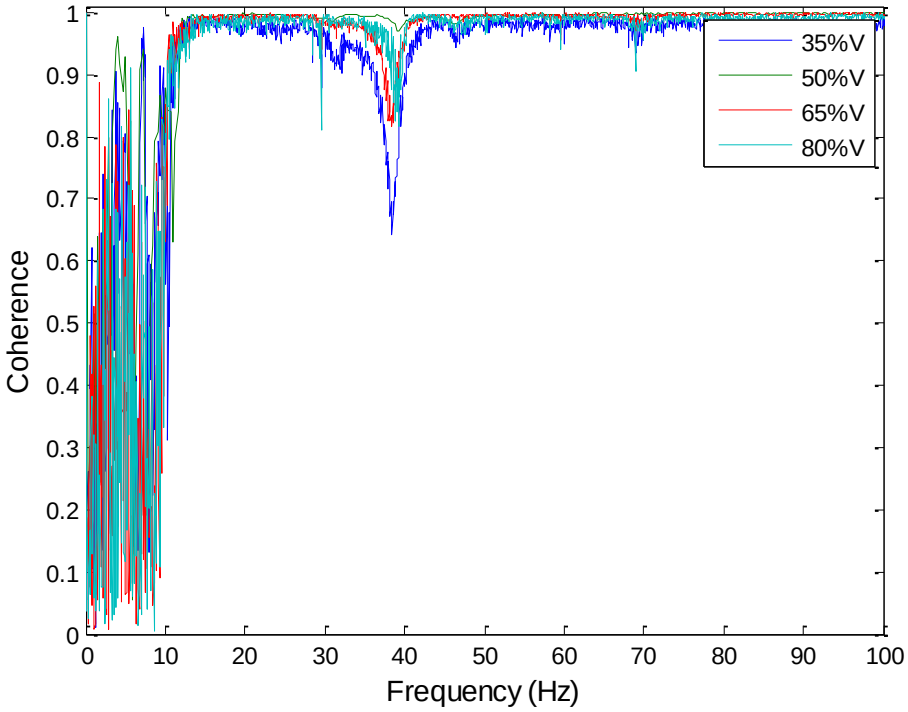

Figure 41: Coherence plot of modal tests spanning the height of the airfoil (Figure 14)

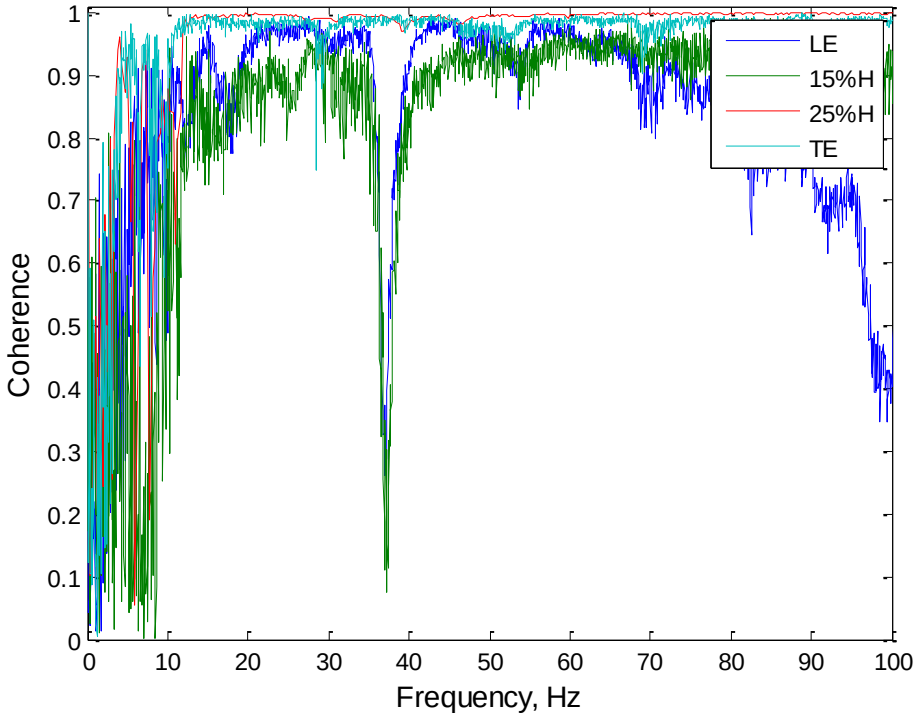

Figure 42: Coherence plot of modal tests spanning the chord of the airfoil (Figure 15)

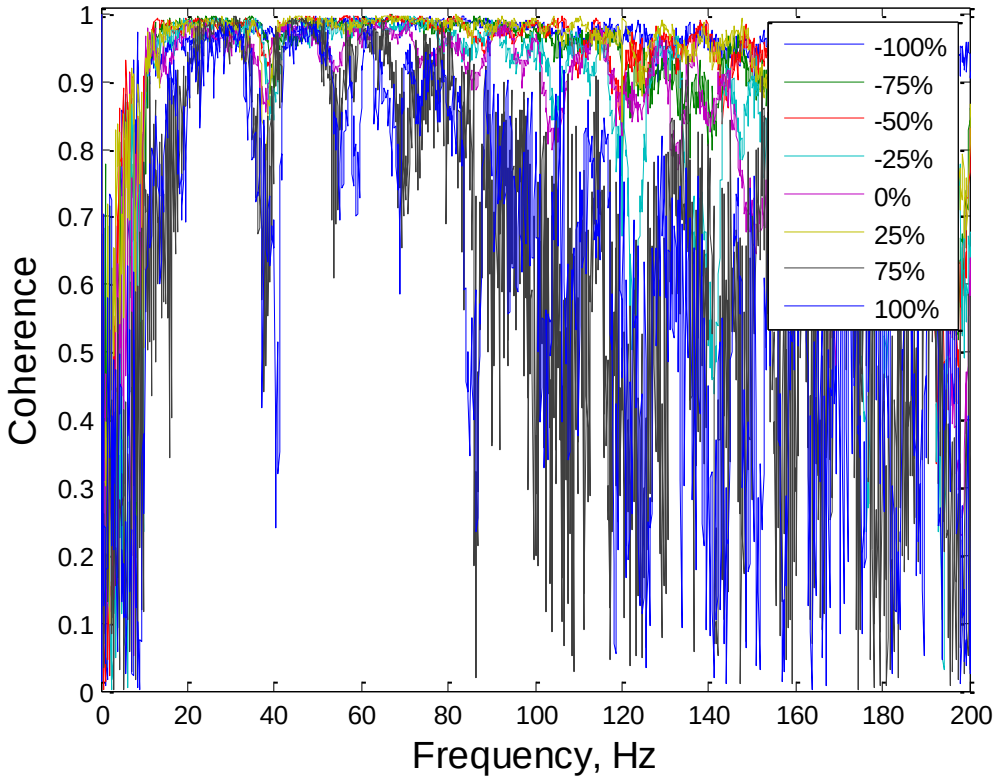

Figure 43: Coherence plot for modal test with actuated airfoil (Figure 16)

Unnormalized Data

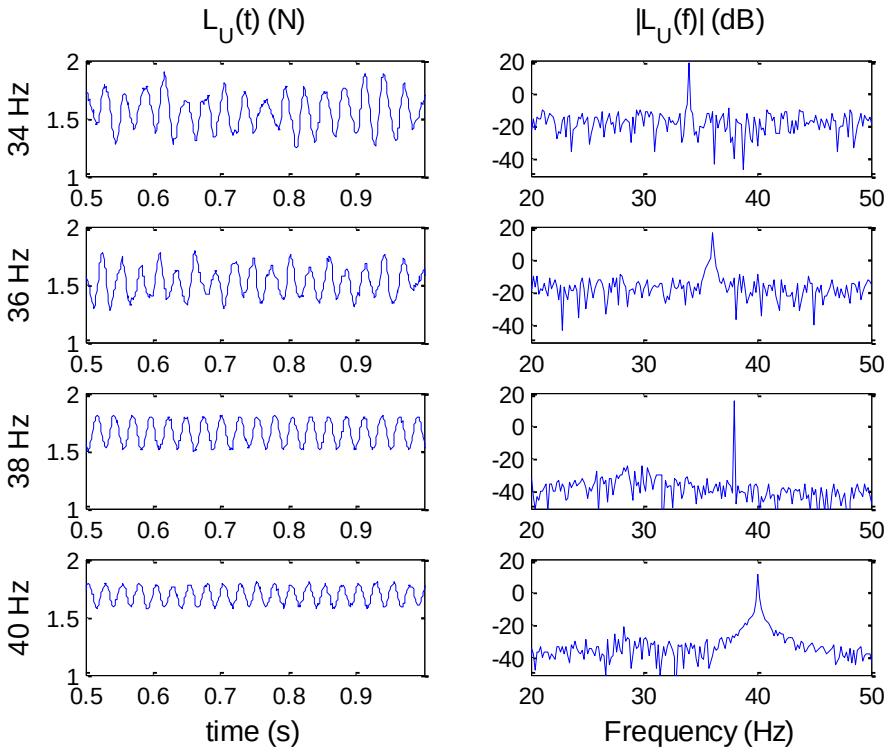

Figure 44: Raw Lift Response from 34-40Hz at V=9 m/s

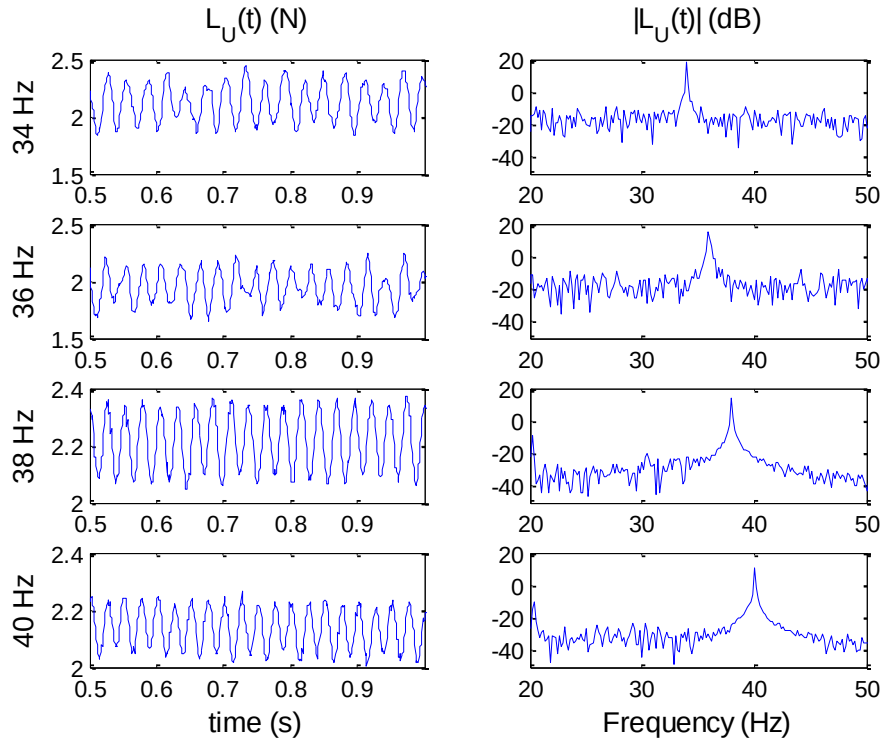

Figure 45: Raw Lift Response from 34-40Hz at V=13 m/s

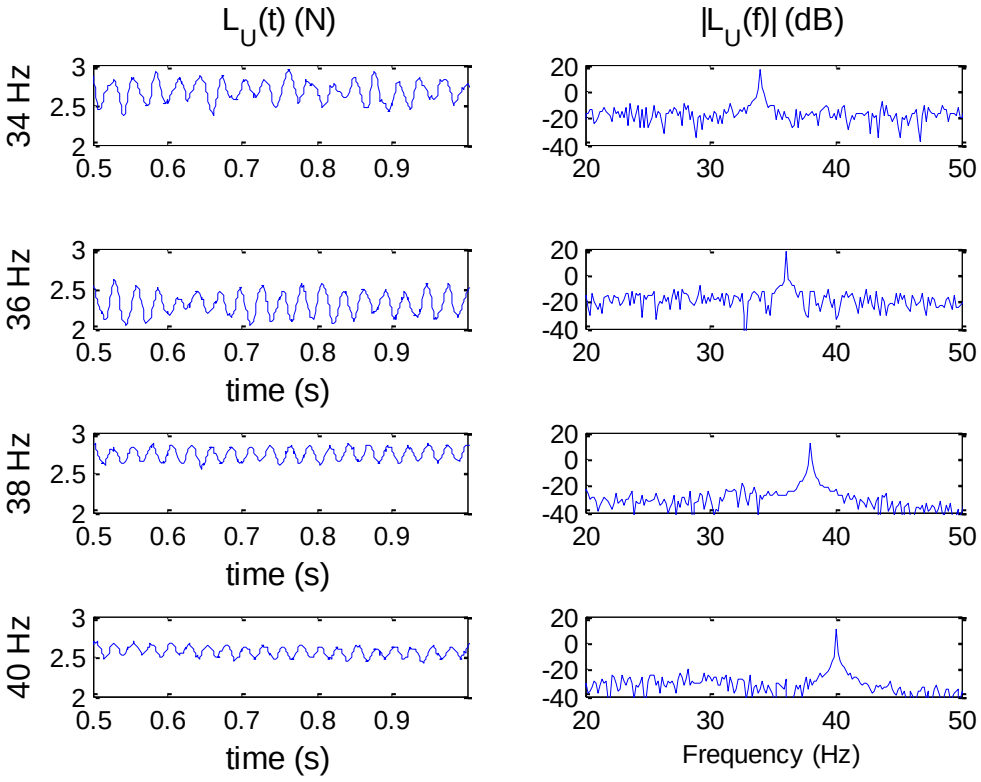

Figure 46: Raw Lift Response from 34-40Hz at V=17 m/s

FRF of Displacement/MFC Input Signal

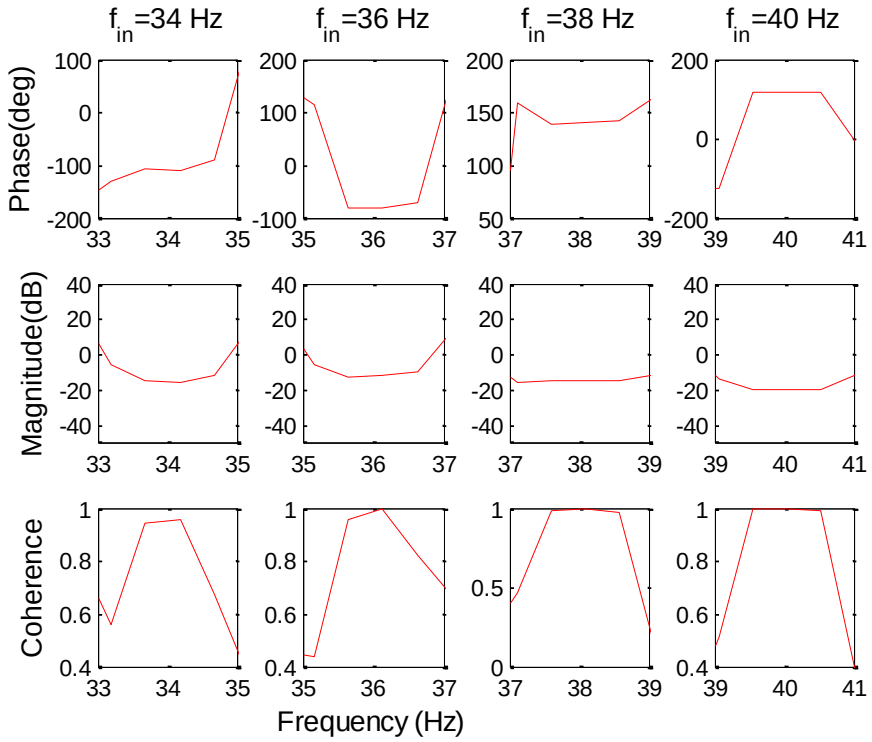

Figure 47: FRF of TE displacement from MFC input signal f_{in}=34-40 Hz at V=0 m/s

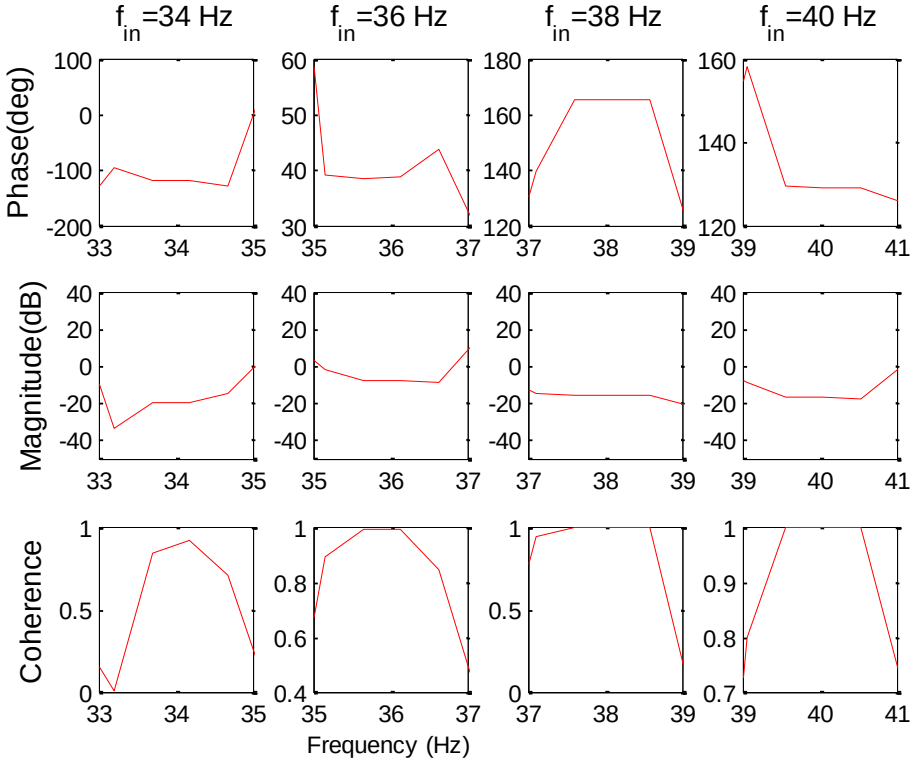

Figure 48: FRF of TE displacement from MFC input signal f_{in}=34-40 Hz at V=9 m/s

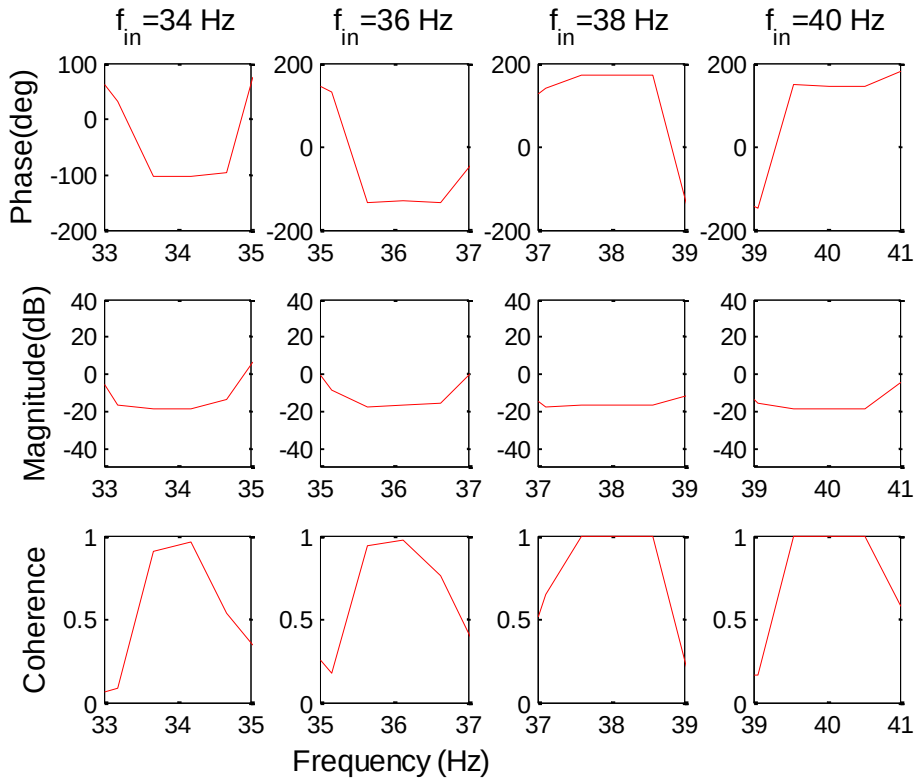

Figure 49: FRF of TE displacement from MFC input signal f_{in} =34-40 Hz at V=13 m/s

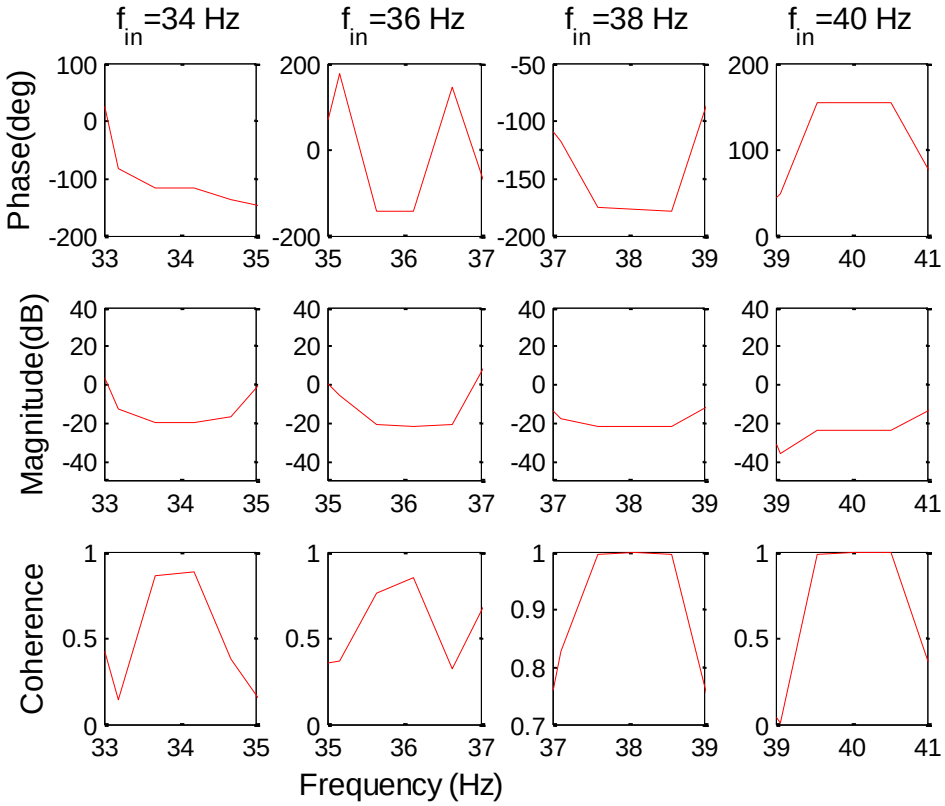

Figure 50: FRF of TE displacement from MFC input signal f_{in} =34-40 Hz at V=17 m/s

FRF of Lift/Displacement

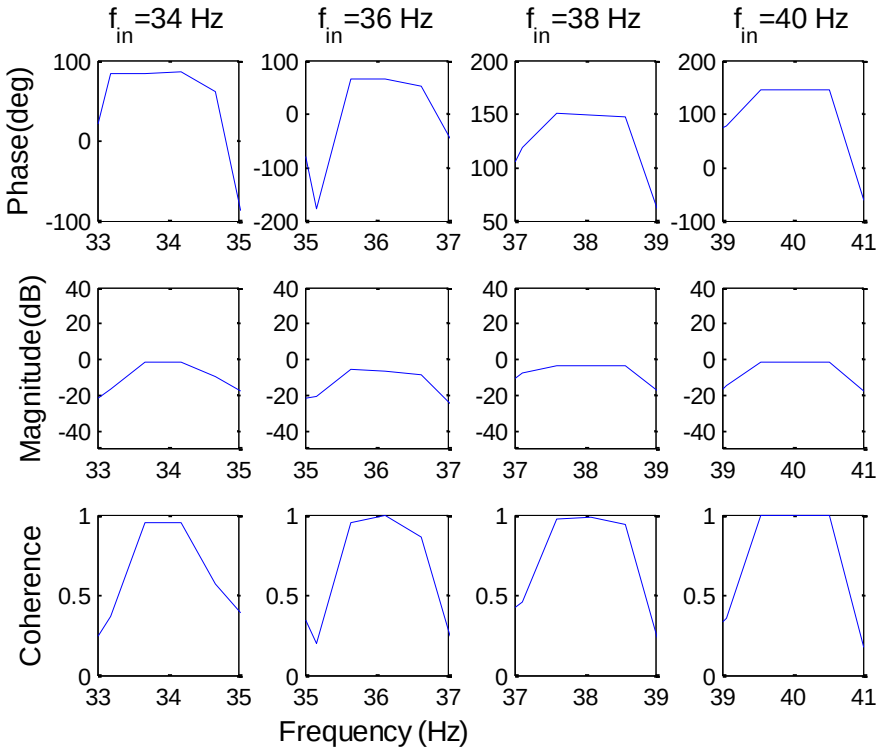

Figure 51: FRF of lift from TE displacement f_{in} =34-40 Hz at V=0 m/s

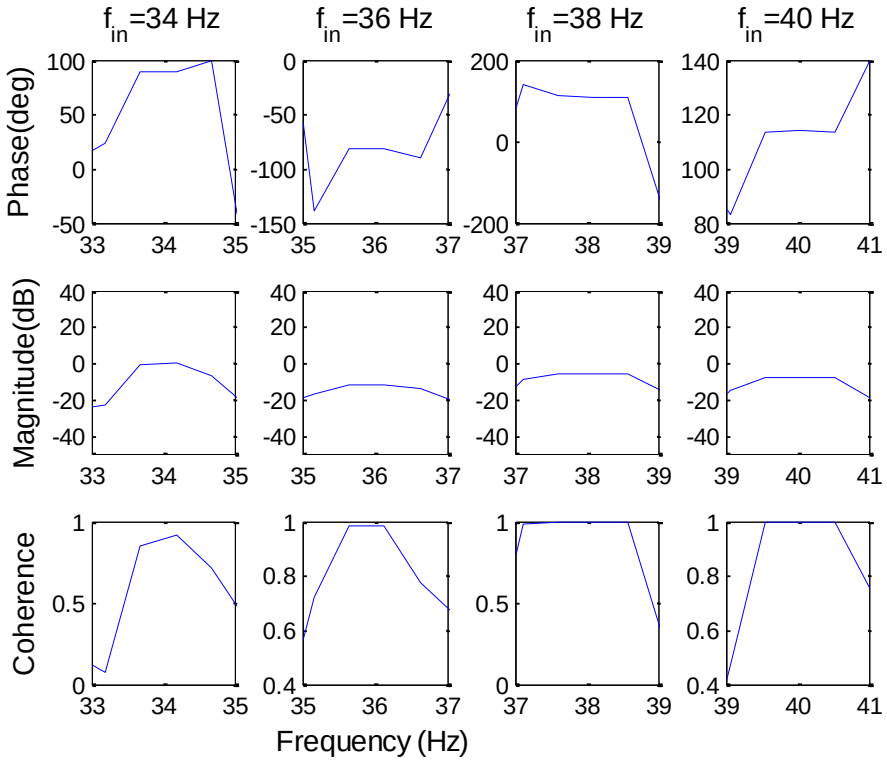

Figure 52: FRF of lift from TE displacement f_{in} =34-40 Hz at V=9 m/s

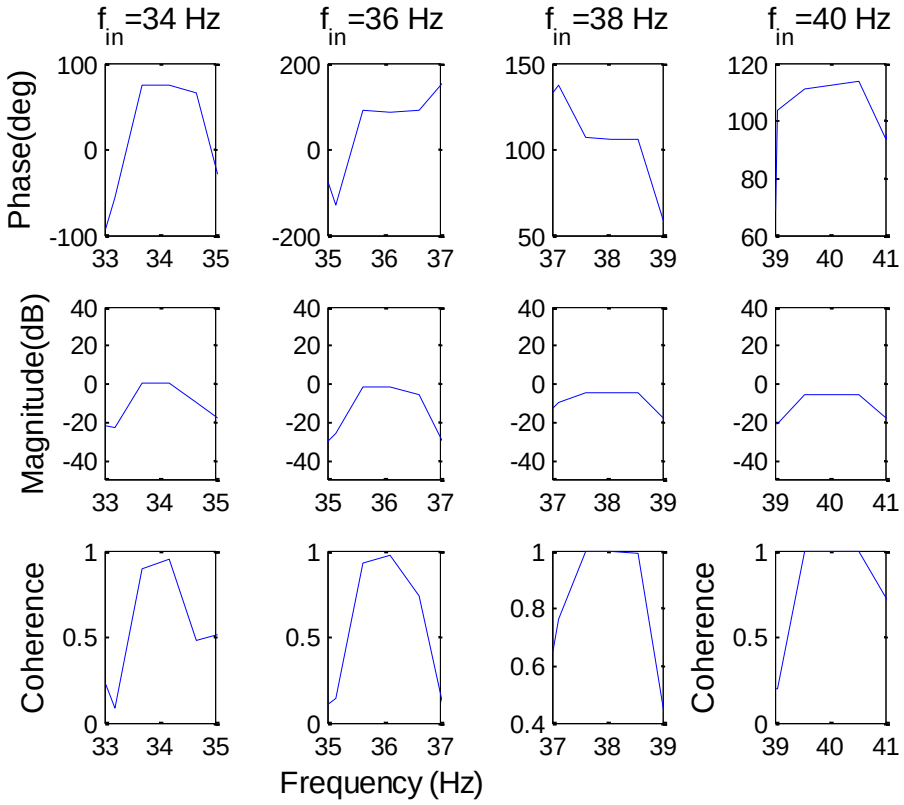

Figure 53: FRF of lift from TE displacement f_{in} =34-40 Hz at V=13 m/s

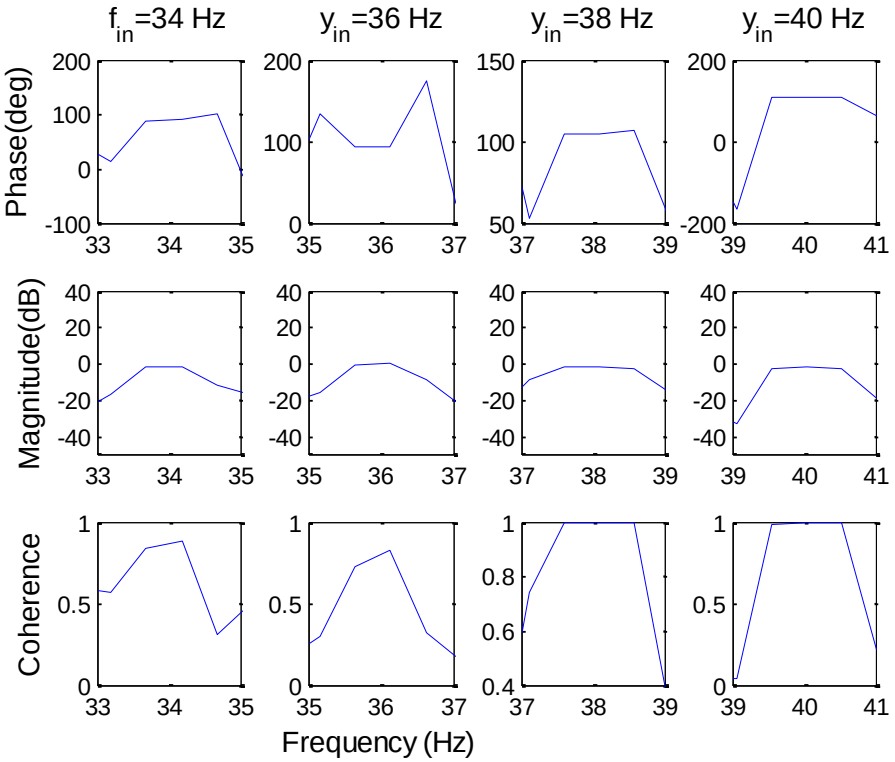

Figure 54: FRF of lift from TE displacement f_{in} =34-40 Hz at V=17 m/s